Hybrid Reconfigurable Intelligent Surface for Integrated Cooperative Localization and Communication for 6G V2X System

Ziyang Lu, Yubin Zhao, *Senior Member, IEEE*, Xiaofan Li, *Senior Member, IEEE*, Huaming Wu, *Senior Member, IEEE*, Cheng-Zhong Xu, *Fellow, IEEE*, and Quan Xue, *Fellow, IEEE*

***Abstract*—Hybrid reconfigurable intelligent surfaces (HRIS) can enable 6G vehicle-to-everything (V2X) system to attain promising localization and communication performance due to its flexible beamforming feature. However, without jointly designing the HRIS control and system resource allocation scheme, the HRIS-V2X system can not adapt to the dynamic environment efficiently. In addition, the optimization of HRIS reflectivity and communication time slice are both non convex and nonlinear problems. In this paper, we propose an asynchronous time division multiplexing (ATDM) protocol for the HRIS-V2X system to meet integrated localization and communications requirements. We analyze the role of HRIS in signal transmission according to squared position error bound (SPEB) and achievable rate (AR). Then, we propose an adaptive block coordinate descent (ABCD) algorithm to optimize the localization accuracy and channel transmission capability, which includes two parts: the time optimization and the reflectivity optimization. Time optimization employs the iterative projection method to find the optimal time slice scheme satisfying AR constraints. Reflectivity optimization uses the Adagrad method with an adaptive learning rate to gradually achieve the optimal reflectivity scheme. The simulation results indicate that our proposed ABCD algorithm has achieved a maximum 94.1% reduction in SPEB compared to greedy algorithm, genetic algorithm (GA), artificial rabbits optimization (ARO) and particle swarm optimization (PSO).**

***Index Terms*—Cooperative localization, hybrid reconfigurable intelligent surface, integrated sensing and communication, Vehicle-to-Everything.**

Received 19 December 2024; revised 30 October 2025; accepted 25 December 2025. Date of publication 30 December 2025; date of current version 7 May 2026. This work was supported in part by the Key Project of National Natural Science Foundation of China under Grant 62431010 and in part by the National Nature Science Foundation of China under Grant 62171484. Recommended for acceptance by S. Zhang. *(Xiaofan Li is the co-first author.) (Corresponding author: Yubin Zhao.)*

Ziyang Lu and Quan Xue are with the School of Electronic and Information Engineering, South China University of Technology, Guangzhou 510640, China (e-mail: luzy@scut.edu.cn; eeqxue@scut.edu.cn).

Yubin Zhao is with the School of Microelectronics Science and Technology, Sun Yat-Sen University, Zhuhai 519082, China (e-mail: zhaoyb23@mail.sysu.edu.cn).

Xiaofan Li is with the School of Intelligent System Science and Engineering, Jinan Unniversity, Zhuhai 519070, China (e-mail: lixiaofan@jnu.edu.cn).

Huaming Wu is with the Center for Applied Mathematics, Tianjin University, Tianjin 300072, China (e-mail: whming@tju.edu.cn).

Cheng-Zhong Xu is with the State Key Lab of IoTSC and Department of Computer and Information Science, University of Macau, Macau 999078, China (e-mail: czxu@um.edu.mo).

Digital Object Identifier 10.1109/TMC.2025.3649173

I. Introduction

In 6G vehicle-to-everything (V2X) technology, integrated cooperative localization and communication are the cornerstone of services [1], [2]. Firstly, integrated cooperative localization technology achieves precise perception and localization of vehicles and the environment by integrating multiple sensors and communication methods. Integrated cooperative localization technology improve the localization accuracy of vehicles in complex environments, reduce dependence on satellite signals, and enhance the robustness of the system [3]. Accurate localization information is the key to ensure driving safety in autonomous driving and intelligent transportation systems [4]. In autonomous driving scenarios, vehicles need to obtain real-time accurate location information of themselves and their surrounding environment to ensure driving safety [5]. Secondly, 6G communication technology provides a high-speed and reliable channel for information transmission among vehicles and between vehicles and infrastructure [6]. Communication technology is the foundation for achieving cooperative control, data sharing, and real-time information transmission in the V2X networks [7]. In highway and urban congestion scenarios, vehicles achieve cooperative control through communication technology, reducing accident risks and improving road traffic efficiency [8]. In summary, integrated cooperative localization and communication plays a crucial role in 6G V2X [9].

Reconfigurable intelligent surface is an emerging wireless communication technology that dynamically regulates propagation paths and characteristics of electromagnetic waves by embedding many programmable reflective units on the surface [10]. The core concept of RIS is to improve communication performance by changing the amplitude and phase of the incident signal or reduce interference within the target area. In wireless communication, RIS is used to optimize channels, especially with significant advantages in high-frequency signal transmission. In addition, RIS can help to provide high-precision localization services by precisely controlling the propagation path of signals. According to the types of RIS unit, RIS is classified into two categories, which are active RIS and passive RIS. For active RIS, each RIS unit is equipped with a power amplifier and a phase control to jointly adapt the amplitude and phase of the reflected signal. The wireless signal is significantly improved by the active RIS, but the power consumption is high.

For passive RIS, only phase control is used for the reflected signal. In this case, the improvement is limited. However, passive RIS is energy efficient due to the passive devices are employed. Recently hybrid reconfigurable intelligent surface (HRIS) is introduced, in which only parts of the units are active while others are passive. HRIS considers the trade-off between performance improvement and energy efficiency. technology is regarded as one of the key technologies for improving the performance of V2X systems [11]. Since HRIS offers hybrid reflection and absorption control scheme, which classic RIS lacks, it can be virtual anchor and reshape the signal power for both of the communication and localization. By collaboratively designing the controlling scheme and the network protocol, HRIS can significantly improve the key metrics of 6G V2X.

However, applying HRIS to 6G V2X systems poses 3 challenges due to the high mobility and dynamic features. First, conventional channel models are not for HRIS based 6G V2X system, since high vehicle speeds cause fast changes in geometry and blockage. On one hand an HRIS-V2X channel model that captures both of reflection and absorption paths is needed [12]. On the other hand, the fundamental performance evaluation model should be developed, e.g., the Fisher information matrix (FIM) and related squared position error bound (SPEB) based on HRIS channel and Doppler speed of vehicle are required. Second, the network protocol must jointly balance localization and communication performance. This protocol needs to be compatible with HRIS control scheme. In addition, for the high mobility and dynamic environment of V2X system, the network protocol should quickly adapt to the environmental changes while reduce the overhead [13]. In this case, how to allocate the resource for channel estimation, localization and communication properly is challenging. Thirdly, with a given protocol, jointly optimizing the HRIS control and resource allocation are high-dimensional, nonconvex (NP-hard) problems. This calls for scalable algorithms that ensure feasibility and converge reliably.

In this paper, we propose a V2X system assisted by dynamic HRIS (HRIS-V2X). We design the localization and communication protocol for the 6G V2X system. We formulate the the optimal localization accuracy bound which is the square position error bound (SPEB) and the achievable rate (AR) for HRIS-V2X system. Then, we employ the AR as the communication requirement constraint and construct the optimization objective based on SPEB. To solve such non-convex NP programming, we develop the adaptive block coordinate descent (ABCD) algorithm. Overall, the major contributions are summarized as follows.

- We introduce HRIS into the V2X system and design the protocol for the HRIS-V2X system. We consider dynamic HRIS to provide services to vehicles in the system. We design the asynchronous time division multiplexing (ATDM) protocol for the HRIS-V2X localization and communication system, which integrates localization, communication, channel estimation, and parameter modification into each cycle. The proposed protocol meets the communication and localization requirements in the ISAC system and can also adapt to real-time changes brought about by dynamic deployment. We analyze SPEB and AR in the HRIS-V2X system. We consider narrowband geometric near-field scenarios, where multiple single antenna base stations' downlink signals are used to estimate the position of HRIS in the presence of dynamically changing HRIS positions. The deviation in localization will alter the final HRIS reflectance distribution and lead to challenging issues in cooperative localization and communication.
- We conduct a theoretical analysis of cooperative localization and communication in the HRIS-V2X system, and construct the main optimization objective for resource allocation. Here, SPEB refers to the lower limit of unbiased estimation of HRIS position variance, and AR refers to the maximum information transmission rate that a communication system can achieve. In the HRIS-V2X system, SPEB and AR are mutually coupled. Therefore, achieving the optimal HRIS reflectivity and time slice is a non-convex NP programming.
- We propose the ABCD algorithm to solve the non-convex NP problem of optimizing SPEB and AR. We derive the SPEB penalty function problem based on AR constraints, which involves the joint optimization of HRIS reflectivity and time slice. To address the combinatorial nature of the problem, we propose the ABCD algorithm. The ABCD algorithm is divided into two parts: HRIS reflectivity optimization and time slice optimization. In terms of reflectivity optimization, we use the Adagrad gradient descent method to quickly converge the SPEB of the HRIS-V2X system to the optimal value through a dynamic learning rate. In time slice optimization, we use the iterative projection method. We project each time slice into the feasible domain of the total length of the time period. Through continuous iteration, the ABCD algorithm gradually improves the performance of HRIS reflectivity optimization and time slice optimization.

The proposed scheme is evaluated via extensive simulations. Compared with the greedy algorithm, genetic algorithm (GA), artificial rabbits optimization (ARO) and particle swarm optimization (PSO), our proposed ABCD achieves better localization and communication performance. In terms of localization accuracy, the simulation results show that ABCD has achieved a 94.1% reduction in SPEB optimization compared to greedy algorithm, a 91.9% reduction compared to GA, a 91.8% reduction compared to ARO, and a 92.1% reduction compared to PSO algorithm. Meanwhile, we demonstrate that the optimization impacts on SPEB and AR are limited by solely relying on passive phase modulation.

Notations: $\mathbb{C}^{m\times n}$ denotes the complex matrices with m rows and n columns. Meanwhile, $\mathbb{R}^{m\times n}$ denotes the space of $m\times n$ real matrices. $\mathbf{0}$ denotes an all-zero matrix. $\mathbf{1}_{m\times n}$ is the $m\times n$ all-one matrix. The letter j is used to represent $\sqrt{-1}$. $\Re\{\cdot\}$ ($\Im\{\cdot\}$) denotes the real (imaginary) part of a variable. We use $(\cdot)^{\mathrm{T}}$ to denote the transpose matrix, $(\cdot)^{-1}$ denotes the inverse matrix. We define $\lfloor\cdot\rfloor$ as the floor division. $\|\|_1$ is the Manhattan norm. $\|\|$ is the Euclidean norm. $\Pi_{\mathcal{C}}(\cdot)$ is the Euclidean projection onto a vector $\mathcal{C}$. $\mathrm{vec}(\cdot)$ is the vectorization of matrices. $\mathrm{tr}(\cdot)$ is the trace of matrix. $\odot$ is Hadamard product. $\otimes$ is Kronecker product. $\det(\cdot)$ is the determinant of matrix. $[\mathbf{A}]_{[m:n,p:q]}$ is the submatrix obtained by arranging the elements in the mth to nth

rows and the pth to qth columns of $\mathbf{A}$. $[\mathbf{a}]_{[m]}$ is the mth elements of $\mathbf{a}$. $[\mathbf{A}]_{[m,n]}$ is the elements in the mth row and nth column of $\mathbf{A}$. $\mathrm{diag}\{a_1, \ldots, a_N\}$ is the diagonal matrix whose contains $a_1, \ldots, a_N$. ∇ operator represents the first derivative. $\mathbf{A} \succeq \mathbf{B}$ represent that $\mathbf{A} - \mathbf{B}$ is positive semidefinite.

II. Related Work

A. Cooperative Localization

Cooperative localization is an effective way to provide high accurate localization service for V2X network. Cooperative localization transmit ranging signals to each other in a cooperative manner for localization. Numerous achievements have accumulated in theoretical research, scheduling control, and localization algorithms. In terms of theoretical research, Win et al. propose the Cramer-Rao lower bound (CRLB) analysis method based on the equivalent Fisher information matrix (EFIM) [14], [15]. In terms of scheduling control, semidefinite programming (SDP), geometric optimization, and game theory are used to design power allocation strategies with EFIM as the core [15], [16], [17]. In addition, using distributed machine learning for power control in wireless cooperative localization is highly suitable for large-scale networks [18], [19]. For instance, edge-cloud fusion with distributed Kalman filters and spatio-temporal graph propagation improves robustness against noise and topology changes [20], [21]. Moreover, RIS has been leveraged to shape geometry, enable multi-user coding, or minimize squared position error bound (SPEB) by discrete phase and carrier optimization [22], [23]. However, most solutions optimize localization in isolation, rely on static anchors, or lack protocol-level resource control that preserves achievable-rate (AR) feasibility under mobility and blockage. In contrast, our work is base on asynchronous time-division multiplexing (ATDM), which jointly allocates HRIS reflectivity and time slice duration under AR constraints, and has SPEB optimization objectives for high mobility V2X.

B. HRIS for V2X

As an important application for future 6G communications, many researchers combine V2X systems with RIS. Researchers demonstrate that RIS can enhance V2X reliability, capacity, and coverage via vehicle panels for blockage mitigation [24], air to ground (A2G) Internet of Things (IoT) multiplexing [25], real-time software control [26], unmanned aerial vehicles (UAV)-assisted V2X with media access control (MAC) design [27], joint power-reflection-spectrum optimization for vehicle to infrastructure (V2I) [28], visible light communication (VLC)-RIS hybrids [29], and dedicated short range communication (DSRC) compatible V2X analysis [30]. The above V2X systems only use RIS as a relay instead of the V2X system, and RIS does not participate in communication or positioning. Mizmizi et al. employ RIS on vehicle roofs for integrated sensing [31]. Long et al. use a deep deterministic policy gradient (DDPG) scheme to address communication-localization in RIS-assisted 6G V2X [32]. Beyond such relay-style uses, HRIS-centric works estimate HRIS pose jointly with user position and optimize HRIS via auto-diff gradient descent, yet still lack protocol-level joint allocation for communication and positioning [33], [34], [35]. However, in above methods, the impact of communication is considered together with the localization process in the case of asynchronous resource protocols and the system mobility. In contrast, we propose a system that uses mobile HRIS as the localization target, with an algorithm that combines reflectivity and time slice allocation, explicitly balancing the localization and communication performance. Some researchers use RIS as a communication and sensing target for V2X. Li et al. consider a single vehicle STAR-RIS with a fixed data frame and propose two stage beam training plus multidimensional orthogonal matching pursuit (MOMP) scheme to trade off sensing and communication [36]. However, the above study does not address the higher complexity of V2X scenarios with multiple interconnected RIS, and the protocol employs fixed time slices which is not suitable to the high mobility targets. In response, our work focuses on a more complex 6G V2X multi-RIS interconnection, and introduces a flexible time slice mechanism at the protocol layer. In this case, a joint optimization is developed accordingly to both minimize the target positioning error lower bound and the guarantee the achievable data rate for communications.

C. Hris for Isac

Integrated sensing and communication (ISAC) is widely recognized as a promising technology for saving hardware and spectrum resources by combining detection and user communication capabilities within a unified platform [37]. How to use HRIS to achieve ISAC has always been a critical issue. Due to its unique physical structure, HRIS has great advantages in sensory integration. The components on HRIS not only reflects impact signals but also absorbs them [38], [39]. This feedback helps base stations maximize the benefits of using RIS at the cost of additional hardware and energy consumption [40], [41]. HRIS-assisted ISAC can share hardware/spectrum by combining active-passive elements, with deployments and beamforming studied to balance sensing-communication performance [42], [43]. Nassar et al. analyze HRIS-assisted NOMA networks, showing that enhanced backscatter improves overall throughput and strengthens sensing-communication integration [44]. Liao et al. design robust HRIS-aided ISAC beamforming that maximizes the minimum sensing beam-pattern gain under SNR/BS/active-element power constraints [45]. Hao et al. develop an HRIS-based mmWave ISAC scheme that jointly maximizes worst-case illumination power and total achievable rate subject to communication QoS [46]. However, above ISAC solutions remain synchronous and beamforming-centric, which is not flexible to the dynamic environment. In contrast, our method runs at the protocol layer, performs AR joint allocation for SPEB through the ABCD algorithm, and can be extended to dynamic HRIS.

III. System Model

A. System Structure

The HRIS-V2X system architecture consists of fixed base stations, mobile HRIS, and vehicles. According to Fig. 1,

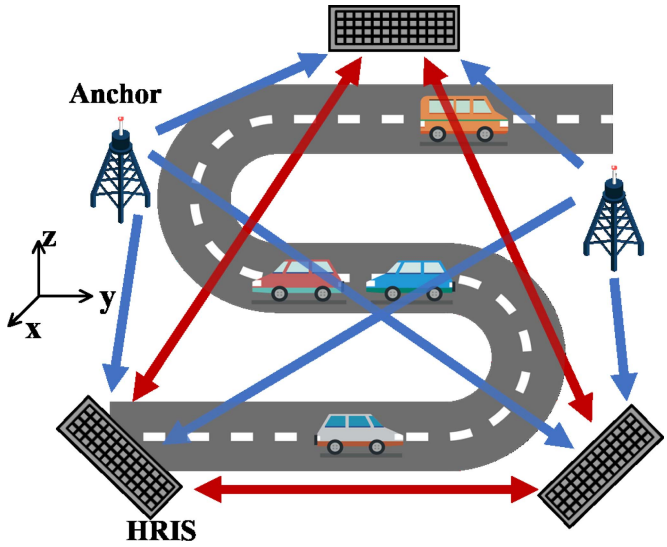

Fig. 1. HRIS-V2X system schematic diagram. fixed base stations dynamically network with mobile HRIS to provide services for vehicles. Vehicles play a service-oriented role in the HRIS-V2X system and do not participate in network localization and communication.

we consider the downlink of the communication and localization system with N_A single antenna base stations and N_T HRIS. The anchors refer to base stations and HRISes are the targets. The wth anchor is located at coordinate $\mathbf{a}_w \in \mathbb{R}^{3\times 1}$. The coordinate vector of anchors is represented as $\mathbf{a} = [\mathbf{a}_1{}^{\mathrm{T}}, \mathbf{a}_2{}^{\mathrm{T}}, \ldots, \mathbf{a}_w{}^{\mathrm{T}}, \ldots, \mathbf{a}_{N_A}{}^{\mathrm{T}}]^{\mathrm{T}}$, $w \in \mathcal{N}_{\mathcal{A}} = \{1, \ldots, N_A\}$. For anchors whose positions are fixed and known. The signal vector emitted by each anchor is $\mathbf{s} = [s_1, \ldots, s_w, \ldots, s_{N_A}]^{\mathrm{T}}$. The reference reflective unit of the HRIS refers to the bottom left corner reflective unit. We set the reference reflective unit of the ith HRIS is initially located at coordinate $\mathbf{p}_i \in \mathbb{R}^{3\times 1}$. The coordinate vector of HRIS is expressed as $\mathbf{p} = [\mathbf{p}_1{}^{\mathrm{T}}, \mathbf{p}_2{}^{\mathrm{T}}, \ldots, \mathbf{p}_i{}^{\mathrm{T}}, \ldots, \mathbf{p}_{N_T}{}^{\mathrm{T}}]^{\mathrm{T}}$, $i \in \mathcal{N}_{\mathcal{T}} = \{1, \ldots, N_T\}$. Each HRIS has an arbitrary but known array geometry, and the coordinate of each HRIS will change over time, and base stations are unaware of this change. We set the ith HRIS moves with a velocity vector $\overrightarrow{\mathbf{v_i}}$, and the x-axis vector and y-axis vector in the ith HRIS array are $\overrightarrow{\mathbf{l_i}}$ and $\overrightarrow{\mathbf{u_i}}$, respectively. Each HRIS comprising N_{row} rows and N_{col} columns reflective units. We set the reflectivity and phase of the ith HRIS are $\boldsymbol{\rho}_i \in \mathbb{R}^{N_{row}\times N_{col}}$ and $\boldsymbol{\psi}_i \in \mathbb{R}^{N_{row}\times N_{col}}$, respectively. The reflective units in HRIS are divided into two types: passive reflective units and active reflective units. In this system, the passive reflective unit has a reflectivity $\rho = 1$ and reflects signals. Meanwhile, the active reflective unit has a reflectivity of $\rho = 0$ and is used for receiving signals. The main parameters of the system are summarized in Table I.

We consider the localization of the mobile HRIS in the V2X system and the downlink communication to vehicles. Therefore, the localization and communication quality of the HRIS are unknown factors that need to be estimated. In addition to traditional static settings, we also consider the possibility of HRIS position changing over time. The channel of the system will time-varying due to the movement of the HRIS. Therefore, we investigate the impact of moving HRIS on the communication quality and localization performance of HRIS-V2X system.

TABLE I
SUMMARY OF NOTATIONS

Symbol	Description
$\mathcal{N}_{\mathcal{A}}$, N_A	Anchor set and its size
$\mathcal{N}_{\mathcal{T}}$, N_T	HRIS set and number of asynchronous time-division multiplexing (ATDM) slices
T, Δt_i	ATDM cycle length and ith slice duration
$\boldsymbol{\rho}_i$, $\boldsymbol{\psi}_i$	Reflectivity and phase of ith HRIS
$\mathbf{p}$, $\mathbf{a}$	HRIS and anchor position
$\mathbf{s}, G_a, G_g, n$	The signal vector, the antenna gain of anchor and HRIS, and the path loss exponent
N_{row}, N_{col}	The number of rows and columns of the reflective units
c, f_c, f, B, λ	The light speed, the carrier frequency, frequency, bandwidth, wavelength c/f_c
$\overrightarrow{\mathbf{v_i}}$, $\overrightarrow{\mathbf{l_i}}$, $\overrightarrow{\mathbf{u_i}}$	The velocity vector, the x-axis vector and y-axis vector in the ith HRIS array
$h_{wi}^{[0]}$, $h_{wi}^{[k]}$	The LoS path channel and the NLoS path channel passing through the kth HRIS between the wth anchor and the ith HRIS
$d_{wi}^{[0]}$, $d_{wi}^{[k]}$	The distance between the wth anchor and the ith HRIS, the distance between the kth and the ith HRIS
$\boldsymbol{\varrho}_{wi}^{[0]}$, $\boldsymbol{\varrho}_{wi}^{[k]}$	The phase of the signal from the wth anchor and the kth HRIS that is incident on the ith HRIS
$\boldsymbol{\hbar}_i$	The time-varying channel vector for the ith HRIS
$J(\mathbf{p})$	Fisher information matrix for $\mathbf{p}$
$\mathcal{P}(\mathbf{p})$	Squared position error bound $\mathrm{tr}(J^{-1})$
R_i, R	Achievable rate in slice i, minimum per-slice rate requirement
$\check{\mathbf{y}}$, $\hat{\mathbf{y}}$, $\mathbf{C}_{\hat{\mathbf{y}}}$	The ideal signal and actual observed signal vectors of all HRIS, covariance matrix
SNR, σ^2	Signal-to-noise ratio; noise power
v, f_D	Vehicle speed; Doppler shift v/λ
T_c	Coherence time (e.g., $0.423/f_D$)
η, ϵ, β_i	Adagrad step size, error, penalty weight
N_i, N_u	Number of ABCD algorithm iterations and the number of population size

B. Asynchronous Time Division Multiplexing Protocol

We design the localization and communication protocol for the HRIS-V2X system, which integrates localization, communication, channel estimation, and parameter modification into each cycle. In each cycle T, the localization and communication protocol of the HRIS-V2X system is shown in Fig. 2. Considering that adjusting the reflectivity and phase of HRIS at high frequencies will cause extremely high energy consumption, we only adjust HRIS before the end of each cycle T. Each cycle contains N_T time slices $\triangle t$, and each time slice corresponds to the HRIS of each unknown localization, where $\sum_{i=1}^{N_T} \triangle t_i = T$. The ith HRIS first performs channel estimation and localization at time t_i. Subsequently, the ith HRIS receives data from all anchors in time slices $\triangle t_i$. Therefore, in order to ensure communication quality and localization performance, we need to adjust all the time slice $\triangle t_i$, HRIS reflectivity $\boldsymbol{\rho}_i$, and HRIS phase $\boldsymbol{\psi}_i$, where

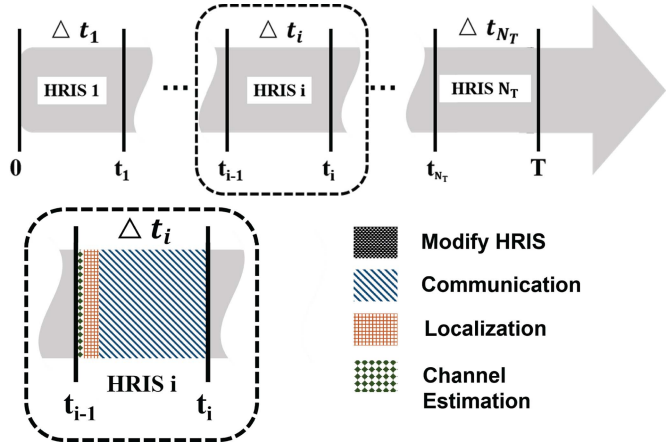

Fig. 2. Schematic diagram of localization and communication protocol for HRIS-V2X system. Within each cycle, each HRIS performs channel estimation, localization, and communication. Adjust the reflectivity and time slice of all HRIS at the end of the cycle.

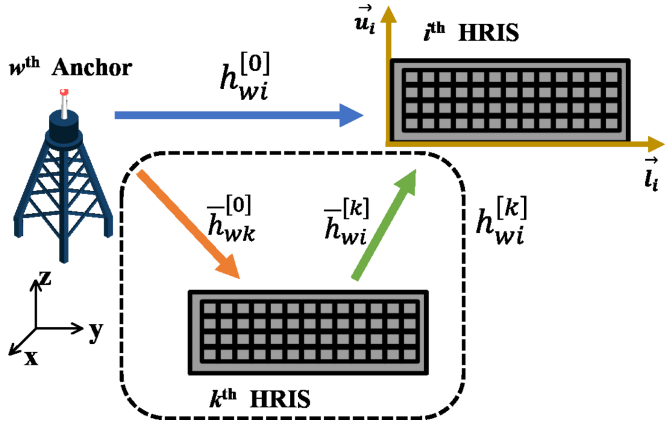

Fig. 3. Schematic diagram of the channel from the wth anchor to the ith HRIS. The blue $h_{wi}^{[0]}$ represents the LoS channel from the wth anchor to the ith HRIS. The dashed box represents the NLoS channel from the wth anchor to the ith HRIS passing through the kth HRIS.

$i \in \mathcal{N}_{\mathcal{T}}$. In the HRIS-V2X system, we use a nonblind estimation method for channel estimation. The nonblind estimation method has been widely used in wireless communication systems due to its high estimation accuracy and relatively low implementation complexity. In the system model, nonblind estimation methods are implemented through three steps. Firstly, as a base station, the anchor sends a known training sequence or slice symbol as a reference signal, which contains the information required for channel estimation. Secondly, after receiving these reference signals, HRIS uses them for initial channel estimation. By comparing the difference between the transmitted reference signal and the received signal, the characteristics of the channel are inferred. Finally, when sending useful information data, the receiving end will make adjustments and updates using the initial channel estimation results to achieve an accurate estimation of the real-time channel.

C. Propagation Model

There are N_A anchors and N_T HRIS in the HRIS-V2X system. We assume that there are at least 2 paths between the anchor and the HRIS. Path $k = 0$ corresponds to the line of sight (LoS) path between the anchor and the HRIS, while the path $k \neq 0$ corresponds to the nonline of sight (NLoS) path between the anchor and HRIS through the kth HRIS. The signal path originating from natural scattering or natural reflection has a much weaker intensity compared to the direct path and HRIS assisted path. Non HRIS paths are eliminated by collecting signals in two stages: first, turn off HRIS to collect signals from non HRIS paths, and then turn on HRIS to collect signals from non HRIS paths and HRIS paths. By comparing the signals from the two stages, isolate HRIS path signals and identify LoS path signals. Thus, this paper will ignore these additional natural scattering or natural reflective signal pathways. Each path corresponds to a channel. Fig. 3 is a schematic diagram of the channel from the wth anchor to the ith HRIS. The blue $h_{wi}^{[0]}$ represents the LoS channel from the wth anchor to the ith HRIS. The dashed box represents the NLoS channel from the wth anchor to the ith HRIS passing through the kth HRIS. According to Fig. 3, the LoS path channel between the wth anchor and the ith HRIS as $h_{wi}^{[0]}(t)$:

$$h_{wi}^{[0]}(t)=\frac{c\sqrt{G_a G_g}}{f_c\left(4\pi d_{wi}^{[0]}\right)^n}\left\|vec\left(\left(\mathbf{1}_{N_{row}\times N_{col}}-\boldsymbol{\rho}_i\right)\odot e^{j\boldsymbol{\varrho}_{wi}^{[0]}}\right)\right\|_1, \tag{1}$$

where $\boldsymbol{\varrho}_{wi}^{[0]} \in \mathbb{R}^{N_{row}\times N_{col}}$ is the phase of the wth anchor signal incident on the ith HRIS, $\Pi_{\mathcal{C}}(\cdot)$ is the Euclidean projection onto a vector $\mathcal{C}$. The element of $\boldsymbol{\varrho}_{wi}^{[0]}$ is described as:

$$\left[\boldsymbol{\varrho}_{wi}^{[0]}\right]_{[l,u]} = 2\pi f_c\left(\lambda\Pi_{\overrightarrow{\mathbf{d}_{wi}^{[0]}}}\left((l-1)\,\overrightarrow{\mathbf{l_i}}+(u-1)\,\overrightarrow{\mathbf{u_i}}\right)\right.$$
$$\left.-\Pi_{\overrightarrow{\mathbf{d}_{wi}^{[0]}}}\left(\overrightarrow{\mathbf{v_i}}\right)t-d_{wi}^{[0]}\right)/c, \tag{2}$$

where $l \in \mathcal{N}_{row} = \{1,\ldots,N_{row}\}$ and $u \in \mathcal{N}_{col} = \{1,\ldots,N_{col}\}$. Meanwhile, the NLoS path channel passing through the kth HRIS between the wth anchor and the ith HRIS as $h_{wi}^{[k]}(t)$:

$$h_{wi}^{[k]}(t) = \bar{h}_{wk}^{[0]}(t)\bar{h}_{wi}^{[k]}(t), \tag{3}$$

where $\bar{h}_{wk}^{[0]}(t)$ is the channel reflected by the kth HRIS of the wth anchor, and $\bar{h}_{wi}^{[k]}(t)$ is the channel from the kth HRIS to the ith HRIS:

$$\begin{cases}\bar{h}_{wi}^{[0]}(t)=\frac{c\sqrt{G_a G_g}}{f_c\left(4\pi d_{wi}^{[0]}\right)^n}\left\|vec\left(\boldsymbol{\rho}_i\odot e^{j\left(\boldsymbol{\varrho}_{wi}^{[0]}+\boldsymbol{\psi}_i\right)}\right)\right\|_1\\ \bar{h}_{wi}^{[k]}(t)=\frac{c\sqrt{G_g G_g}}{f_c\left(4\pi d_{wi}^{[k]}\right)^n}\left\|vec\left(\left(\mathbf{1}_{N_{row}\times N_{col}}-\boldsymbol{\rho}_i\right)\odot e^{j\boldsymbol{\varrho}_{wi}^{[k]}}\right)\right\|_1\end{cases}, \tag{4}$$

where $\boldsymbol{\varrho}_{wi}^{[k]} \in \mathbb{R}^{N_{row}\times N_{col}}$ is the phase of the kth HRIS signal incident on the ith HRIS. The element of $\boldsymbol{\varrho}_{wi}^{[k]} \in \mathbb{R}^{N_{row}\times N_{col}}$ is

described as:

$$\left[\boldsymbol{\varrho}_{wi}^{[k]}\right]_{[l,u]} = 2\pi f_c \left(\lambda \Pi_{\overrightarrow{\mathbf{d}_{wi}^{[k]}}} \left((l-1)\,\overrightarrow{\mathbf{l_i}} + (u-1)\,\overrightarrow{\mathbf{u_i}}\right) + \Pi_{\overrightarrow{\mathbf{d}_{wi}^{[k]}}} \left(\overrightarrow{\mathbf{v_k}} - \overrightarrow{\mathbf{v_i}}\right) t - d_{wi}^{[k]}\right)/c, \quad (5)$$

where $l \in \mathcal{N}_{row} = \{1, \ldots, N_{row}\}$ and $u \in \mathcal{N}_{col} = \{1, \ldots, N_{col}\}$. For the ith HRIS, the time-varying channel vector $\boldsymbol{\hbar}_i(t)$ from all anchor is described as:

$$\boldsymbol{\hbar}_i(t) = \left[\sum_{k \neq i}^{N_T} h_{wi}^{[k]}(t) + h_{wi}^{[0]}(t)\right]_{w=1}^{N_A}. \quad (6)$$

D. Achievable Rate

According to Fig. 2, in the ideal entire time cycle T, the received signal energy of the ith HRIS is:

$$\int_0^T \left|[\boldsymbol{\hbar}_i(t)]_{[i]}\right|^2 \mathrm{d}t = \underbrace{\int_{\sum_{m=1}^{i-1} \triangle t_m}^{\sum_{m=1}^{i} \triangle t_m} \left|[\boldsymbol{\hbar}_i(t)]_{[i]}\right|^2 \mathrm{d}t}_{\text{desired signal energy}} + \underbrace{\sum_{k \neq i}^{N_T} \int_{\sum_{m=1}^{k-1} \triangle t_m}^{\sum_{m=1}^{k} \triangle t_m} \left|[\boldsymbol{\hbar}_i(t)]_{[i]}\right|^2 \mathrm{d}t}_{\text{interference energy}}, \quad (7)$$

where the received signal energy of the ith HRIS is divided into two parts: desired signal energy and interference energy. The desired signal energy refers to the signal energy of the ith HRIS in time slice $\triangle t_i$, which is used for signal transmission. At the same time, interference energy refers to the signal energy of the ith HRIS $\triangle t_k$, $k \neq i$, which is the interference energy brought by communication with other HRIS. For the ith HRIS, only signals from time slice $\triangle t_i$ are needed, while signals from other time slices are not needed.

Achievable rate refers to the maximum information transmission rate that a communication system achieves under specific conditions. Realizable rate is an important indicator for measuring the performance of communication systems. Therefore, based on (7), the implementation rate of the ith HRIS (in bits/s/Hz/bandwith) is obtained:

$$R_i = \log_2\left(1 + \frac{\int_{\sum_{m=1}^{i-1} \triangle t_m}^{\sum_{m=1}^{i} \triangle t_m} \left|[\boldsymbol{\hbar}_i(t)]_{[i]}\right|^2 \mathrm{d}t}{\sum_{k \neq i}^{N_T} \int_{\sum_{m=1}^{k-1} \triangle t_m}^{\sum_{m=1}^{k} \triangle t_m} \left|[\boldsymbol{\hbar}_i(t)]_{[i]}\right|^2 \mathrm{d}t}\right). \quad (8)$$

E. Spatial Position Error Bound

According to Fig. 2, each HRIS will be located at the corresponding time point. The ideal signal vectors used for localization by all HRIS are represented as:

$$\breve{\mathbf{y}} = \left[\boldsymbol{\hbar}_1(0)^{\mathrm{T}}\mathbf{s}, \boldsymbol{\hbar}_2(\triangle t_1)^{\mathrm{T}}\mathbf{s}, \ldots, \boldsymbol{\hbar}_{N_T}\left(\sum_{i=1}^{N_T-1} \triangle t_i\right)^{\mathrm{T}}\mathbf{s}\right]^{\mathrm{T}}, \quad (9)$$

where the signal vector $\breve{\mathbf{y}} \in \mathbb{C}^{N_T \times 1}$ is an imaginary vector. Both real and imaginary parts of a signal contain HRIS localization information, so a complex signal vector $\breve{\mathbf{y}} \in \mathbb{C}^{N_T \times 1}$ is converted into a real vector $\tilde{\mathbf{y}} \in \mathbb{R}^{2N_T \times 1}$:

$$\tilde{\mathbf{y}} = \left[\Re\left\{[\breve{\mathbf{y}}]_{[t]}\right\}; \Im\left\{[\breve{\mathbf{y}}]_{[t]}\right\}\right]_{t=1}^{\mathrm{N_T}}. \quad (10)$$

The noise appeared in HRIS and channel in the system. On a localization model with additive noise, if the HRIS coordinate vector is a reference node, its coordinate estimation vector $\hat{\mathbf{p}}$ is represented as $\hat{\mathbf{p}} = \mathbf{p} + \mathbf{b}$,where $\mathbf{b}$ is the range measurement error vector. Meanwhile, in the localization model with additional noise, the actual observed signal vector $\hat{\mathbf{y}}$ received by HRIS is represented as: $\hat{\mathbf{y}} = \tilde{\mathbf{y}} + \mathbf{n}$, where the vector $\mathbf{n}$ is the complex additive Gaussian noise. Therefore, the actual observed signal vector $\hat{\mathbf{y}}$ is a real Gaussian random vector with a covariance matrix of $\mathbf{C}$. For the condition of coordinate vector $\mathbf{p}$, the probability density function of the actual observed signal vector $\hat{\mathbf{y}}$ is:

$$f(\hat{\mathbf{y}} \mid \mathbf{p}) = \frac{\exp\left(-\frac{1}{2}(\hat{\mathbf{y}} - \tilde{\mathbf{y}})^{\mathrm{T}}\mathbf{C}_{\hat{\mathbf{y}}}^{-1}(\hat{\mathbf{y}} - \tilde{\mathbf{y}})\right)}{(2\pi)^{N_T}\left[\det\left(\mathbf{C}_{\hat{\mathbf{y}}}\right)\right]^{\frac{1}{2}}}. \quad (11)$$

HRIS coordinate is estimated based on $\hat{\mathbf{y}}$, and the corresponding localization accuracy is quantified based on the mean square error (MSE) between the actual coordinate $\mathbf{p}$ and the estimated coordinate vector $\hat{\mathbf{p}}$. If $\hat{\mathbf{p}}$ represents the unbiased estimate of $\mathbf{p}$, we obtain the lower bound of the MSE matrix as follows:

$$\mathbb{E}\left\{(\hat{\mathbf{p}} - \mathbf{p})(\hat{\mathbf{p}} - \mathbf{p})^{\mathrm{T}}\right\} \succeq \mathbf{J}(\mathbf{p})^{-1}, \quad (12)$$

where $\mathbf{J}(\mathbf{p})$ is the Fisher information matrix of the HRIS coordinate vector $\mathbf{p}$, which is given by:

$$\mathbf{J}(\mathbf{p}) \triangleq \frac{1}{2}\,\mathrm{tr}\left(\mathrm{C}_{\hat{\mathbf{y}}}^{-1}\frac{\partial \mathrm{C}_{\hat{\mathbf{y}}}}{\partial \mathbf{p}}\mathrm{C}_{\hat{\mathbf{y}}}^{-1}\frac{\partial \mathrm{C}_{\hat{\mathbf{y}}}}{\partial \mathbf{p}}\right) + \frac{\partial \tilde{\mathbf{y}}^{\mathrm{T}}}{\partial \mathbf{p}}\mathrm{C}_{\hat{\mathbf{y}}}^{-1}\frac{\partial \tilde{\mathbf{y}}}{\partial \mathbf{p}}. \quad (13)$$

We assume that the receive signal $\hat{\mathbf{y}}$ are independent to each others, and $\mathrm{C}_{\hat{\mathbf{y}}} = \mathrm{diag}\{{\sigma_1}^2, \ldots, {\sigma_{N_T}}^2\}$ is independent with coordinate vector, $\frac{\partial \mathrm{C}_{\hat{\mathbf{y}}}}{\partial \mathbf{p}} = 0$. Meanwhile, we assume that $\sigma_1 = \sigma_2 = \cdots = \sigma_{N_T} = \sigma$. Therefore, the submatrix of FIM $\mathbf{J}(\mathbf{p})$ in (13) is represented as

$$[\mathbf{J}(\mathbf{p})]_{[3i-2:3i,3k-2:3k]} = \frac{\partial \tilde{\mathbf{y}}^{\mathrm{T}}}{\partial \mathbf{p}_i}\frac{\partial \tilde{\mathbf{y}}}{\partial \mathbf{p}_k}\sigma^2, \quad (14)$$

where σ is variance of noise; $\frac{\partial \tilde{\mathbf{y}}}{\partial \mathbf{p}_i} \in \mathbb{R}^{2N_T \times 3}$ is the Jacobian matrix of the partial derivative of the observed signal vector $\partial \tilde{\mathbf{y}}$ to the ith taerget coordinate $\mathbf{p}_i$:

$$\frac{\partial \tilde{\mathbf{y}}}{\partial \mathbf{p}_i} = \left[\Re\left\{\nabla_{\mathbf{p}_i}\boldsymbol{\hbar}_1(0)^{\mathrm{T}}\mathbf{s}\right\}, \Im\left\{\nabla_{\mathbf{p}_i}\boldsymbol{\hbar}_1(0)^{\mathrm{T}}\mathbf{s}\right\}, \ldots, \Re\left\{\nabla_{\mathbf{p}_i}\boldsymbol{\hbar}_{N_T}(t_{N_T-1})^{\mathrm{T}}\mathbf{s}\right\}, \Im\left\{\nabla_{\mathbf{p}_i}\boldsymbol{\hbar}_{N_T}(t_{N_T-1})^{\mathrm{T}}\mathbf{s}\right\}\right]^{\mathrm{T}}, \quad (15)$$

where $\nabla_{\mathbf{p}_i}\boldsymbol{\hbar}_k$ is the partial derivative vector of the channel vector $\boldsymbol{\hbar}_k$ to the coordinate $\mathbf{p}_i$. In general, all submatrices of the FIM in (14) are written by $\nabla_{\mathbf{p}_i}\boldsymbol{\hbar}_k(t)^{\mathrm{T}}\mathbf{s}$. The $\nabla_{\mathbf{p}_i}\boldsymbol{\hbar}_k(t)^{\mathrm{T}}\mathbf{s} \in \mathbb{R}^{3\times 1}$ is the partial derivative vector of the kth HRIS channel vector

subjected to the position coordinate $\mathbf{p}_i$. When $x \in \{1,2,3\}$ and $k \neq i$, the xth element of $\nabla_{\mathbf{p}_i}\hbar_k(t)^{\mathrm{T}}\mathbf{s} \in \mathbb{R}^{3\times 1}$ is expressed as:

$$\left[\nabla_{\mathbf{p}_i}\hbar_k(t)^{\mathrm{T}}\mathbf{s}\right]_{[x]} = \sum_{w=1}^{N_A} s_w \nabla_{[\mathbf{p}_i]_{[x]}} h_{wk}^{[i]}(t). \tag{16}$$

Based on (3), $\nabla_{[\mathbf{p}_i]_{[x]}} h_{wk}^{[i]}(t)$ is represented as:

$$\begin{aligned}\nabla_{[\mathbf{p}_i]_{[x]}} h_{wk}^{[i]}(t) = {} & \nabla_{[\mathbf{p}_i]_{[x]}} \bar{h}_{wi}^{[0]}(t)\bar{h}_{wk}^{[i]}(t) \\ & + \bar{h}_{wi}^{[0]}(t)\nabla_{[\mathbf{p}_i]_{[x]}} \bar{h}_{wk}^{[i]}(t),\end{aligned} \tag{17}$$

where the entries in $\nabla_{[\mathbf{p}_i]_{[x]}} \bar{h}_{wi}^{[0]}(t)$ is:

$$\begin{aligned}\nabla_{[\mathbf{p}_i]_{[x]}} \bar{h}_{wi}^{[0]}(t) = {} & \frac{-n\bar{h}_{wi}^{[0]}(t)\left[\boldsymbol{\Xi}_{wi}^{[0]}\right]_{[x]}}{d_{wi}^{[0]}} + \frac{c\sqrt{G_a G_g}}{f_c\left(4\pi d_{wi}^{[0]}\right)^n} \\ & \left\| vec\left(\boldsymbol{\rho}_i \odot e^{j\left(\boldsymbol{\varrho}_{wi}^{[0]} + \boldsymbol{\psi}_i\right)} \odot j\nabla_{[\mathbf{p}_i]_{[x]}} \boldsymbol{\varrho}_{wi}^{[0]}\right)\right\|_1,\end{aligned} \tag{18}$$

and $\nabla_{[\mathbf{p}_i]_{[x]}} \bar{h}_{wk}^{[i]}(t)$ is:

$$\begin{aligned}\nabla_{[\mathbf{p}_i]_{[x]}} \bar{h}_{wk}^{[i]}(t) = {} & \frac{n\bar{h}_{wk}^{[i]}(t)\left[\boldsymbol{\Xi}_{wk}^{[i]}\right]_{[x]}}{d_{wk}^{[i]}} + \frac{c\sqrt{G_g G_g}}{f_c\left(4\pi d_{wk}^{[i]}\right)^n} \\ & \left\| vec\left(\left(\mathbf{1}_{N_{row}\times N_{col}} - \boldsymbol{\rho}_k\right) \odot e^{j\boldsymbol{\varrho}_{wk}^{[i]}} \odot j\nabla_{[\mathbf{p}_i]_{[x]}} \boldsymbol{\varrho}_{wk}^{[i]}\right)\right\|_1,\end{aligned} \tag{19}$$

where $\nabla_{[\mathbf{p}_i]_{[x]}} \boldsymbol{\varrho}_{wi}^{[0]}$ and $\nabla_{[\mathbf{p}_i]_{[x]}} \boldsymbol{\varrho}_{wk}^{[i]}$ are partial derivative vector of phase $\boldsymbol{\varrho}_{wi}^{[0]}$ and $\boldsymbol{\varrho}_{wk}^{[i]}$ to the coordinate element $[\mathbf{p}_i]_{[x]}$. The description of $\nabla_{[\mathbf{p}_i]_{[x]}} \boldsymbol{\varrho}_{wi}^{[0]}$ and $\nabla_{[\mathbf{p}_i]_{[x]}} \boldsymbol{\varrho}_{wk}^{[i]}$ are (20) and (21), shown at the bottom of this page, which both posted on top of next page.

Vector $\boldsymbol{\Xi}_{wi}^{[0]}$ and $\boldsymbol{\Xi}_{wk}^{[i]}$ are the direction vectors of $\overrightarrow{\mathbf{d}_{wi}^{[0]}}$ and $\overrightarrow{\mathbf{d}_{wk}^{[i]}}$, respectively. The vectors $\boldsymbol{\Theta}_{\overrightarrow{\mathbf{l}_\mathbf{k}}}$ and $\boldsymbol{\Theta}_{\overrightarrow{\mathbf{u}_\mathbf{k}}}$ are the horizontal and vertical vectors of the ith HRIS:

$$\boldsymbol{\Xi}_{wi}^{[0]} = \left[\cos\phi_{\overrightarrow{\mathbf{d}_{wi}^{[0]}}} \sin\varphi_{\overrightarrow{\mathbf{d}_{wi}^{[0]}}}, \sin\phi_{\overrightarrow{\mathbf{d}_{wi}^{[0]}}} \sin\varphi_{\overrightarrow{\mathbf{d}_{wi}^{[0]}}}, \cos\varphi_{\overrightarrow{\mathbf{d}_{wi}^{[0]}}}\right]^{\mathrm{T}}, \tag{22}$$

$$\boldsymbol{\Xi}_{wk}^{[i]} = \left[\cos\phi_{\overrightarrow{\mathbf{d}_{wk}^{[i]}}} \sin\varphi_{\overrightarrow{\mathbf{d}_{wk}^{[i]}}}, \sin\phi_{\overrightarrow{\mathbf{d}_{wk}^{[i]}}} \sin\varphi_{\overrightarrow{\mathbf{d}_{wk}^{[i]}}}, \cos\varphi_{\overrightarrow{\mathbf{d}_{wk}^{[i]}}}\right]^{\mathrm{T}}, \tag{23}$$

$$\boldsymbol{\Theta}_{\overrightarrow{\mathbf{l}_\mathbf{i}}} = \left[\cos\phi_{\overrightarrow{\mathbf{l}_\mathbf{i}}} \sin\varphi_{\overrightarrow{\mathbf{l}_\mathbf{i}}}, \sin\phi_{\overrightarrow{\mathbf{l}_\mathbf{i}}} \sin\varphi_{\overrightarrow{\mathbf{l}_\mathbf{i}}}, \cos\varphi_{\overrightarrow{\mathbf{l}_\mathbf{i}}}\right]^{\mathrm{T}}, \tag{24}$$

$$\boldsymbol{\Theta}_{\overrightarrow{\mathbf{u}_\mathbf{i}}} = \left[\cos\phi_{\overrightarrow{\mathbf{u}_\mathbf{i}}} \sin\varphi_{\overrightarrow{\mathbf{u}_\mathbf{i}}}, \sin\phi_{\overrightarrow{\mathbf{u}_\mathbf{i}}} \sin\varphi_{\overrightarrow{\mathbf{u}_\mathbf{i}}}, \cos\varphi_{\overrightarrow{\mathbf{u}_\mathbf{i}}}\right]^{\mathrm{T}}. \tag{25}$$

Meanwhile, when $k = i$, the xth element of $\nabla_{\mathbf{p}_i}\hbar_i(t)^{\mathrm{T}}\mathbf{s} \in \mathbb{R}^{3\times 1}$ is expressed as:

$$\left[\nabla_{\mathbf{p}_i}\hbar_i(t)^{\mathrm{T}}\mathbf{s}\right]_{[x]} \sum_{w=1}^{N_A}\sum_{k\neq i}^{N_T} s_w\left(\nabla_{[\mathbf{p}_i]_{[x]}} h_{wi}^{[k]}(t) + \nabla_{[\mathbf{p}_i]_{[x]}} h_{wi}^{[0]}(t)\right). \tag{26}$$

where x represents the dimension of coordinates, $x \in \{1,2,3\}$. Based on the expression of $h_{wi}^{[k]}(t)$ on (3), $\nabla_{[\mathbf{p}_i]_{[x]}} h_{wi}^{[k]}(t)$ is represented as:

$$\nabla_{[\mathbf{p}_i]_{[x]}} h_{wi}^{[k]}(t) = \bar{h}_{wk}^{[0]}(t)\nabla_{[\mathbf{p}_i]_{[x]}} \bar{h}_{wi}^{[k]}(t), \tag{27}$$

where the entries in $\nabla_{[\mathbf{p}_i]_{[x]}} \bar{h}_{wi}^{[k]}(t)$ is manifested as:

$$\begin{aligned}\nabla_{[\mathbf{p}_i]_{[x]}} \bar{h}_{wi}^{[k]}(t) = {} & \frac{-n\bar{h}_{wi}^{[k]}(t)\left[\boldsymbol{\Xi}_{wi}^{[k]}\right]_{[x]}}{d_{wi}^{[k]}} + \frac{c\sqrt{G_g G_g}}{f_c\left(4\pi d_{wi}^{[k]}\right)^n} \\ & \left\| \mathrm{vec}\left(\left(\mathbf{1}_{N_{row}\times N_{col}} - \boldsymbol{\rho}_i\right) \odot e^{j\boldsymbol{\varrho}_{wi}^{[k]}} \odot j\nabla_{[\mathbf{p}_i]_{[x]}} \boldsymbol{\varrho}_{wi}^{[k]}\right)\right\|_1,\end{aligned} \tag{28}$$

where the description of $\nabla_{[\mathbf{p}_i]_{[x]}}[\boldsymbol{\varrho}_{wi}^{[k]}]_{[l,u]}$ is (29) shown at the bottom of the next page.

Therefore, the lower bound of MSE between the actual coordinate $\mathbf{p}$ and the estimated coordinate $\hat{\mathbf{p}}$ is

$$\mathbb{E}\left\{\|\hat{\mathbf{p}} - \mathbf{p}\|^2\right\} \geq \mathrm{tr}\left\{\mathbf{J}\left(\mathbf{p}\right)^{-1}\right\} \triangleq \mathcal{P}\left(\mathbf{p}\right), \tag{30}$$

where $\mathbf{J}(\mathbf{p})$ is the Fisher information matrix (FIM) and $\mathcal{P}(\mathbf{p})$ is the SPEB of HRIS. SPEB refers to the lower limit of unbiased estimation of HRIS position variance.

IV. Problem Formulation

In the ATDM symbol transmission wireless localization network with cycle T, due to limited communication resources, the ith HRIS will locate itself at time t_i and receive data from all anchors in time period $\triangle t_i$, respectively. We assume that HRIS is adjusted only before the end of each cycle. We have imposed

$$\begin{aligned}\nabla_{[\mathbf{p}_i]_{[x]}}\left[\boldsymbol{\varrho}_{wi}^{[0]}\right]_{[l,u]} = {} & 2\pi f_c\lambda\left(-\Pi_{\overrightarrow{\mathbf{d}_{wi}^{[0]}}}\left((l-1)\overrightarrow{\mathbf{l}_\mathbf{i}} + (u-1)\overrightarrow{\mathbf{u}_\mathbf{i}}\right)\left[\boldsymbol{\Xi}_{wi}^{[0]}\right]_{[x]} + (l-1)\left[\boldsymbol{\Theta}_{\overrightarrow{\mathbf{l}_\mathbf{i}}}\right]_{[x]} + (u-1)\left[\boldsymbol{\Theta}_{\overrightarrow{\mathbf{u}_\mathbf{i}}}\right]_{[x]} + \right) / \left(d_{wi}^{[0]}c\right) \\ & + 2\pi f_c\left(t\Pi_{\overrightarrow{\mathbf{d}_{wi}^{[0]}}}\left(\overrightarrow{\mathbf{v}_\mathbf{i}}\right)\left[\boldsymbol{\Xi}_{wi}^{[0]}\right]_{[x]} - t\left\|\overrightarrow{\mathbf{v}_\mathbf{i}}\right\|\left[\boldsymbol{\Theta}_{\overrightarrow{\mathbf{v}_\mathbf{i}}}\right]_{[x]} - d_{wi}^{[0]}\left[\boldsymbol{\Xi}_{wi}^{[0]}\right]_{[x]}\right) / \left(d_{wi}^{[0]}c\right),\end{aligned} \tag{20}$$

$$\begin{aligned}\nabla_{[\mathbf{p}_i]_{[x]}}\left[\boldsymbol{\varrho}_{wk}^{[i]}\right]_{[l,u]} = {} & 2\pi f_c\lambda\left(\Pi_{\overrightarrow{\mathbf{d}_{wk}^{[i]}}}\left((l-1)\overrightarrow{\mathbf{l}_\mathbf{k}} + (u-1)\overrightarrow{\mathbf{u}_\mathbf{k}}\right)\left[\boldsymbol{\Xi}_{wk}^{[i]}\right]_{[x]} - (l-1)\left[\boldsymbol{\Theta}_{\overrightarrow{\mathbf{l}_\mathbf{k}}}\right]_{[x]} - (u-1)\left[\boldsymbol{\Theta}_{\overrightarrow{\mathbf{u}_\mathbf{k}}}\right]_{[x]} + \right) / \left(d_{wk}^{[i]}c\right) \\ & + 2\pi f_c\left(t\Pi_{\overrightarrow{\mathbf{d}_{wk}^{[i]}}}\left(\overrightarrow{\mathbf{v}_\mathbf{k}} - \overrightarrow{\mathbf{v}_\mathbf{k}}\right)\left[\boldsymbol{\Xi}_{wk}^{[i]}\right]_{[x]} - t\left\|\overrightarrow{\mathbf{v}_\mathbf{i}} - \overrightarrow{\mathbf{v}_\mathbf{k}}\right\|\left[\boldsymbol{\Theta}_{\overrightarrow{\mathbf{v}_\mathbf{k}} - \overrightarrow{\mathbf{v}_\mathbf{k}}}\right]_{[x]} + d_{wk}^{[i]}\left[\boldsymbol{\Xi}_{wk}^{[i]}\right]_{[x]}\right) / \left(d_{wk}^{[i]}c\right).\end{aligned} \tag{21}$$

a constraint R on the communication achievable rate of each HRIS. The achievable rate of each HRIS must be greater than AR constraint $R_i \geq R,\ \forall i \in \mathcal{N}_{\mathcal{T}}$ to prevent a few high-information HRIS from monopolizing resources, otherwise network lifetime and localization accuracy deteriorate. Through the simulation in Section VII, we find that the phase modulation of HRIS has no significant impact on the HRIS-V2X system. Therefore, in each cycle T, in order to ensure communication quality and localization performance, we need to adjust the time slice $\triangle\mathbf{t}$, HRIS reflectivity $\boldsymbol{\rho}$ simultaneously:

$$(\mathbb{P}_1): \min_{\boldsymbol{\rho},\triangle\mathbf{t}} \ \mathcal{P}\left(\mathbf{p}|\boldsymbol{\rho},\triangle\mathbf{t}\right) \tag{31}$$

$$\text{s.t. } C1: \forall \boldsymbol{\rho} \in \{0,1\}, \tag{31a}$$

$$C2: \sum_{i=1}^{N_T} \triangle t_i = T, \tag{31b}$$

$$C3: R_i \geq R,\ \forall i \in \mathcal{N}_{\mathcal{T}}, \tag{31c}$$

Where $\boldsymbol{\rho} = [\boldsymbol{\rho_1}, \ldots, \boldsymbol{\rho_{N_T}}]$ represents the reflectance matrix of HRIS, and $\triangle\mathbf{t} = [\triangle t_1, \ldots, \triangle t_{N_T}]^{\mathrm{T}}$ represents the time slice vector of HRIS. The purpose of constraint (31a) is to balance the time consumption of the HRIS. The purpose of constraint (31b) is to constrain the lower bound of achievable rate while ensuring the reliability of communication and localization at each HRIS. Due to $\mathbb{P}_1$ is a nonlinear and non-convex problem, matrix inversion operations require a significant amount of resources and time. According to the inequality relationship, SPEB $\mathcal{P}(\mathbf{p})$ in (30) is equivalent to:

$$\frac{3N_T}{\mathcal{P}\left(\mathbf{p}|\boldsymbol{\rho},\triangle\mathbf{t}\right)} \leq \frac{1}{3N_T}\sum_{i=1}^{3N_T} \varsigma_i = \frac{\mathrm{tr}\left\{\mathbf{J}\left(\mathbf{p}|\boldsymbol{\rho},\triangle\mathbf{t}\right)\right\}}{3N_T}, \tag{32}$$

where ς_i is the ith eigenvalue of Fisher information matrix (FIM) $\mathbf{J}(\mathbf{p}|\boldsymbol{\rho},\triangle\mathbf{t})$. Therefore, $\mathbb{P}_1$ is relaxed as $\mathbb{P}_2$:

$$(\mathbb{P}_2): \max_{\boldsymbol{\rho},\triangle\mathbf{t}} \ \mathrm{tr}\left[\mathbf{J}\left(\mathbf{p}|\boldsymbol{\rho},\triangle\mathbf{t}\right)\right] \tag{33}$$

$$\text{s.t. } C1 - C3 \tag{33a}$$

Furthermore, $\mathbb{P}_2$ is difficult to solve as variables $\boldsymbol{\Psi}$, $\boldsymbol{\rho}$ and $\triangle\mathbf{t}$ are coupled in both the objective function (33) and constraints $C3$. In the following section, we propose an effective algorithm based on projection method and gradient descent method.

V. Adaptive Block Coordinate Descent Algorithms

The feature of the proposed adaptive block coordinate descent (ABCD) algorithm is to embed a double-loop structure, where the inner loop solves the reflectance problem $\boldsymbol{\rho}$ of HRIS related to $\mathbb{P}_2$, and the outer loop aims to update the time slice $\triangle\mathbf{t}$. To solve the equality constraint, we merge the corresponding AR constraint $C3$ terms into the objective function and obtain the following problem:

$$(\mathbb{P}_3): \min_{\boldsymbol{\rho},\triangle\mathbf{t}} \ \mathcal{L}_\beta = \underbrace{-\mathrm{tr}\left\{\mathbf{J}\left(\boldsymbol{\rho},\triangle\mathbf{t}\right)\right\}}_{\text{main objective function}} + \underbrace{\sum_{i=1}^{N_T} \beta_i^{-(R-R_i)}}_{\text{validation function}} \tag{34}$$

$$\text{s.t. } C1 - C2 \tag{34a}$$

$$C4: \beta_i > 1,\ \forall i \in \mathcal{N}_{\mathcal{T}}, \tag{34b}$$

Where the objective function $\mathcal{L}_\beta$ is divided into two parts: the main objective function, and the validation function that excludes non compliant constraints. Variables $\boldsymbol{\rho}$ and $\triangle\mathbf{t}$ are separable in constraints and only coupled in the objective function (34). Therefore, with fixed penalty parameters β_i, we solve the $\mathbb{P}_3$ by applying the ABCD algorithm. We optimize the main objective function and the validation function in $\mathbb{P}_3$ as subproblems. Specifically, we suggest dividing $\mathbb{P}_3$ into two blocks: $\boldsymbol{\rho}$ and $\triangle\mathbf{t}$, and alternately optimize one block while keeping the other blocks fixed. Each ABCD algorithm iteration used to solve $\mathbb{P}_3$ consists of the following two steps: Adagrad gradient descent method and iterative projection.

A. Adagrad Gradient Descent Method for $\boldsymbol{\rho}$

We optimize $\boldsymbol{\rho}$ in parallel in this stage. Because SPEB is more affected by HRIS reflectivity than AR, subproblem main objective function in $\mathbb{P}_3$ is represented as:

$$(\mathbb{P}_3^*): \min_{\boldsymbol{\rho}} \ \mathcal{L}_\beta \tag{35}$$

$$\text{s.t. } C1,\ C4. \tag{35a}$$

The objective function is optimized through the gradient descent method. With $N_T N_{row} N_{col}$ binary units, there are $2^{N_T N_{row} N_{col}}$ reflectivity schemes. Therefore, optimizing the reflectivity of HRIS is an NP problem. To obtain a feasible solution to (35), we adopt Adagrad in the ABCD algorithm. We assume $\boldsymbol{\rho}_i^{n_i} \in \mathbb{R}^{N_{row}\times N_{col}}$ is the the reflectivity of the ith HRIS at the n_ith iteration. For gradient descent method, when the learning rate is too low, objective function converge slowly. When the learning rate is too high, gradient descent method may cause the function to fluctuate at the extreme value. The Adagrad gradient descent method solves the problem of manually adjusting the learning rate in commonly used gradient descent methods. The Adagrad method uses a batch of gradients

$$\begin{aligned}\nabla_{[\mathbf{p}_i]_{[x]}}\left[\boldsymbol{\varrho}_{wi}^{[k]}\right]_{[l,u]} = {} & 2\pi f_c\lambda\left(-\Pi_{\overrightarrow{\mathbf{d}_{wi}^{[k]}}}\left((l-1)\overrightarrow{\mathbf{l_i}} + (u-1)\overrightarrow{\mathbf{u_i}}\right)\left[\boldsymbol{\Xi}_{wi}^{[k]}\right]_{[x]} + (l-1)\left[\boldsymbol{\Theta}_{\overrightarrow{\mathbf{l_i}}}\right]_{[x]} + (u-1)\left[\boldsymbol{\Theta}_{\overrightarrow{\mathbf{u_i}}}\right]_{[x]} + \right) / \left(d_{wi}^{[k]}c\right) \\ & + 2\pi f_c\left(-t\Pi_{\overrightarrow{\mathbf{d}_{wi}^{[k]}}}\left(\overrightarrow{\mathbf{v_k}} - \overrightarrow{\mathbf{v_i}}\right)\left[\boldsymbol{\Xi}_{wi}^{[k]}\right]_{[x]} + t\left\|\overrightarrow{\mathbf{v_k}} - \overrightarrow{\mathbf{v_i}}\right\|\left[\boldsymbol{\Theta}_{\overrightarrow{\mathbf{v_k}}-\overrightarrow{\mathbf{v_i}}}\right]_{[x]} - d_{wi}^{[k]}\left[\boldsymbol{\Xi}_{wi}^{[k]}\right]_{[x]}\right) / \left(d_{wi}^{[k]}c\right).\end{aligned} \tag{29}$$

to accumulate variables $\chi_{i,lu}^{n_i}$, where n_i is the n_ith iteration. Here, $\chi_{i,lu}^{n_i}$ accumulates the squared historical gradients of unit (l,u) of the ith HRIS up to iteration n_i. The attenuation degree of each dimension of the gradient is different. Therefore, the variable $\chi_{i,lu}^{n_i}$ is adaptable. The accumulation variable $\chi_{i,lu}^{n_i}$ is shown as follow:

$$\chi_{i,lu}^{n_i} = \chi_{i,lu}^{n_i-1} + \nabla_{[\boldsymbol{\rho}_i^{n_i}]_{[l,u]}} \operatorname{tr}\left\{\mathbf{J}\left(\boldsymbol{\rho}\right)\right\}^2. \tag{36}$$

The Adagrad gradient descent method modifies the learning rate $\eta_{i,lu}^{n_i}$ of the reflective unit in row l and column u of the kth HRIS at n_ith iteration by accumulate variables $\chi_{k,lu}^{n_i}$:

$$\eta_{i,lu}^{n} = \frac{\eta}{\sqrt{\chi_{i,lu}^{n_i} + \epsilon}}, \tag{37}$$

where ϵ is the error, η is the initial learning rate. Because the accumulate variables $\chi_{i,lu}^{n_i}$ is adaptive to gradients. Therefore, the learning rate $\eta_{i,lu}^{n_i}$ also adapts to the gradient.

The Adagrad method adjusts the learning rate $\eta_{i,lu}^{n_i}$ appropriately through parameter tuning, and the gradient is positively correlated with the update amount. In order to prevent HRIS reflectivity transformation from being too sensitive and affecting convergence, we add a threshold κ that changes the reflectivity of HRIS only when the gradient exceeds the threshold. The reflective unit in row l and column u of the ith HRIS at the n_ith iteration is updated as follows:

$$\left[\boldsymbol{\rho}_i^{n_i+1}\right]_{[l,u]} = \begin{cases} 1, & if\ \eta_{i,lu}^{n_i} \nabla_{[\boldsymbol{\rho}_i^{n}]_{[l,u]}} \operatorname{tr}\left\{\mathbf{J}\left(\boldsymbol{\rho}\right)\right\} \le -\kappa, \\ 0, & if\ \eta_{i,lu}^{n_i} \nabla_{[\boldsymbol{\rho}_i^{n_i}]_{[l,u]}} \operatorname{tr}\left\{\mathbf{J}\left(\boldsymbol{\rho}\right)\right\} \ge \kappa, \\ \left[\boldsymbol{\rho}_i^{n_i}\right]_{[l,u]}, & if\ else. \end{cases} \tag{38}$$

By continuously iterating, the reflectivity $\boldsymbol{\rho}$ is optimized until it exceeds the allowed number of steps. The gradient of reflectivity $\boldsymbol{\rho}$ in $\operatorname{tr}\{\mathbf{J}(\boldsymbol{\rho})\}$ is shown as:

$$\begin{aligned} \nabla_{[\boldsymbol{\rho}_k]_{[l,u]}} \operatorname{tr}\left\{\mathbf{J}\left(\boldsymbol{\rho}\right)\right\} = &\sum_{i=1}^{N_T} \nabla_{[\boldsymbol{\rho}_k]_{[l,u]}} \nabla_{\mathbf{p}_i} \tilde{\mathbf{y}}^{\mathrm{T}} \nabla_{\mathbf{p}_i} \tilde{\mathbf{y}} / \sigma^2 \\ &+ \nabla_{\mathbf{p}_i} \tilde{\mathbf{y}}^{\mathrm{T}} \nabla_{[\boldsymbol{\rho}_k]_{[l,u]}} \nabla_{\mathbf{p}_i} \tilde{\mathbf{y}} / \sigma^2, \end{aligned} \tag{39}$$

where $\nabla_{[\boldsymbol{\rho}_k]_{[l,u]}} \nabla_{\mathbf{p}_i} \tilde{\mathbf{y}}$ is the partial derivative matrix of the Jacobian matrix $\nabla_{\mathbf{p}_i} \tilde{\mathbf{y}}$ for the reflectivity $[\boldsymbol{\rho}_k]_{[l,u]}$ of the reflective unit in row l and column u of the kth HRIS.

According to (15), $\nabla_{[\boldsymbol{\rho}_k]_{[l,u]}} \nabla_{\mathbf{p}_i} \tilde{\mathbf{y}}$ is expressed as:

$$\begin{aligned} \nabla_{[\boldsymbol{\rho}_k]_{[l,u]}} \nabla_{\mathbf{p}_i} \tilde{\mathbf{y}} = &\left[\Re\left\{\nabla_{[\boldsymbol{\rho}_k]_{[l,u]}} \nabla_{\mathbf{p}_i} \hbar_1(t)^{\mathrm{T}} \mathbf{s}\right\},\right. \\ &\left.\Im\left\{\nabla_{[\boldsymbol{\rho}_k]_{[l,u]}} \nabla_{\mathbf{p}_i} \hbar_1(t)^{\mathrm{T}} \mathbf{s}\right\}\right]_{t=0}^{\mathrm{N_T}-1}, \end{aligned} \tag{40}$$

where $\nabla_{[\boldsymbol{\rho}_k]_{[l,u]}} \nabla_{\mathbf{p}_i} \hbar_m(t)^{\mathrm{T}} \mathbf{s} \in \mathbb{R}^{3\times 1}$ is the partial derivative vector of the $\nabla_{\mathbf{p}_i} \hbar_m(t)^{\mathrm{T}} \mathbf{s}$ to the reflectance $[\boldsymbol{\rho}_k]_{[l,u]}$ of the reflective unit in row l and column u of the kth HRIS. When $x \in \{1,2,3\}$, $k \ne i \ne m$, $[\nabla_{[\boldsymbol{\rho}_k]_{[l,u]}} \nabla_{\mathbf{p}_i} \hbar_m(t)^{\mathrm{T}} \mathbf{s}]_{[x]} = 0$. Meanwhile, when $k \ne i = m$, the xth element of $\nabla_{[\boldsymbol{\rho}_k]_{[l,u]}} \nabla_{\mathbf{p}_i} \hbar_i(t)^{\mathrm{T}} \mathbf{s}$ is expressed as:

$$\begin{aligned} &\left[\nabla_{[\boldsymbol{\rho}_k]_{[l,u]}} \nabla_{\mathbf{p}_i} \hbar_i(t)^{\mathrm{T}} \mathbf{s}\right]_{[x]} \\ &= \sum_{w=1}^{N_A} s_w \nabla_{[\boldsymbol{\rho}_k]_{[l,u]}} \bar{h}_{wk}^{[0]}(t) \nabla_{[\mathbf{p}_i]_{[x]}} \bar{h}_{wi}^{[k]}(t), \end{aligned} \tag{41}$$

where the entries in $\nabla_{[\boldsymbol{\rho}_k]_{[l,u]}} \bar{h}_{wk}^{[0]}(t)$ is manifested as:

$$\nabla_{[\boldsymbol{\rho}_k]_{[l,u]}} \bar{h}_{wk}^{[0]}(t) = \frac{c\sqrt{G_a G_g}}{f_c \left(4\pi d_{wk}^{[0]}\right)^n} e^{j\left(\left[\boldsymbol{\varrho}_{wk}^{[0]}\right]_{[l,u]} + [\psi_k]_{[l,u]}\right)}. \tag{42}$$

When $k = i \ne m$, the xth element of $\nabla_{[\boldsymbol{\rho}_i]_{[l,u]}} \nabla_{\mathbf{p}_i} \hbar_m(t)^{\mathrm{T}} \mathbf{s}$ is expressed as (43) shown at the bottom of this page, where the entries in $\nabla_{[\boldsymbol{\rho}_i]_{[l,u]}} \nabla_{[\mathbf{p}_i]_{[x]}} \bar{h}_{wi}^{[0]}(t)$ is manifested as:

$$\begin{aligned} &\nabla_{[\boldsymbol{\rho}_i]_{[l,u]}} \nabla_{[\mathbf{p}_i]_{[x]}} \bar{h}_{wi}^{[0]}(t) = \nabla_{[\boldsymbol{\rho}_i]_{[l,u]}} \bar{h}_{wi}^{[0]}(t) \\ &\left(-n\left[\boldsymbol{\Xi}_{wi}^{[0]}\right]_{[x]} + j d_{wi}^{[0]} \nabla_{[\mathbf{p}_i]_{[x]}} \left[\boldsymbol{\varrho}_{wi}^{[0]}\right]_{[l,u]}\right) / d_{wi}^{[0]}. \end{aligned} \tag{44}$$

When $k \ne i = m$, the xth element of $\nabla_{[\boldsymbol{\rho}_k]_{[l,u]}} \nabla_{\mathbf{p}_i} \hbar_k(t)^{\mathrm{T}} \mathbf{s}$ is expressed as (40) on bottom of next page, where the entries in $\nabla_{[\boldsymbol{\rho}_k]_{[l,u]}} \bar{h}_{wk}^{[i]}(t)$ and $\nabla_{[\boldsymbol{\rho}_k]_{[l,u]}} \nabla_{[\mathbf{p}_i]_{[x]}} \bar{h}_{wk}^{[i]}(t)$ are manifested as:

$$\nabla_{[\boldsymbol{\rho}_k]_{[l,u]}} \bar{h}_{wk}^{[i]}(t) = -\frac{c\sqrt{G_a G_g}}{f_c \left(4\pi d_{wk}^{[i]}\right)^n} e^{j\left[\boldsymbol{\varrho}_{wk}^{[i]}\right]_{[l,u]}}, \tag{46}$$

$$\begin{aligned} &\nabla_{[\boldsymbol{\rho}_k]_{[l,u]}} \nabla_{[\mathbf{p}_i]_{[x]}} \bar{h}_{wk}^{[i]}(t) = \nabla_{[\boldsymbol{\rho}_k]_{[l,u]}} \bar{h}_{wk}^{[i]}(t) \\ &\left(n\left[\boldsymbol{\Xi}_{wk}^{[i]}\right]_{[x]} - j d_{wk}^{[i]} \nabla_{[\mathbf{p}_i]_{[x]}} \left[\boldsymbol{\varrho}_{wk}^{[i]}\right]_{[l,u]}\right) / d_{wk}^{[i]}. \end{aligned} \tag{47}$$

When $k = i = m$, the xth element of $\nabla_{[\boldsymbol{\rho}_i]_{[l,u]}} \nabla_{\mathbf{p}_i} \hbar_i(t)^{\mathrm{T}} \mathbf{s}$ is expressed as (45)–(48) shown at the bottom of the next page, where the entries in $\nabla_{[\boldsymbol{\rho}_i]_{[l,u]}} \nabla_{[\mathbf{p}_i]_{[x]}} \bar{h}_{wi}^{[k]}(t)$ is manifested as:

$$\begin{aligned} &\nabla_{[\boldsymbol{\rho}_i]_{[l,u]}} \nabla_{[\mathbf{p}_i]_{[x]}} \bar{h}_{wi}^{[k]}(t) = \nabla_{[\boldsymbol{\rho}_i]_{[l,u]}} \bar{h}_{wi}^{[k]}(t) \\ &\left(-n\left[\boldsymbol{\Xi}_{wi}^{[k]}\right]_{[x]} + j d_{wi}^{[k]} \nabla_{[\mathbf{p}_i]_{[x]}} \left[\boldsymbol{\varrho}_{wi}^{[k]}\right]_{[l,u]}\right) / d_{wi}^{[k]}, \end{aligned} \tag{49}$$

$$\nabla_{[\boldsymbol{\rho}_i]_{[l,u]}} h_{wi}^{[k]}(t) = -\frac{c\sqrt{G_a G_g}}{f_c \left(4\pi d_{wi}^{[k]}\right)^n} e^{j\left[\boldsymbol{\varrho}_{wi}^{[k]}\right]_{[l,u]}}. \tag{50}$$

B. Iterative Projection for $\triangle\mathbf{T}$

In this step, we optimize $\triangle\mathbf{t}$. According to the expression of (8), the AR is highly dependent on the length of each time slice $\triangle t$. Because AR is more affected by time slices than SPEB. Therefore, we use AR as the main objective to optimize $\triangle\mathbf{t}$,

$$\left[\nabla_{[\boldsymbol{\rho}_i]_{[l,u]}} \nabla_{\mathbf{p}_i} \hbar_m(t)^{\mathrm{T}} \mathbf{s}\right]_{[x]} = \sum_{w=1}^{N_A} s_w \nabla_{[\boldsymbol{\rho}_i]_{[l,u]}} \nabla_{[\mathbf{p}_i]_{[x]}} \bar{h}_{wi}^{[0]}(t) \bar{h}_{wm}^{[i]}(t) + s_w \nabla_{[\boldsymbol{\rho}_i]_{[l,u]}} \bar{h}_{wi}^{[0]}(t) \nabla_{[\mathbf{p}_i]_{[x]}} \bar{h}_{wm}^{[i]}(t), \tag{43}$$

and the validation function in $\mathbb{P}_3$ is simplified into the following subproblem:

$$(\mathbb{P}_3^{**}): \min_{\triangle \mathbf{t}} \ \mathcal{L}_\beta \tag{51}$$

$$\text{s.t. } C2,\ C4 \tag{51a}$$

We optimize the time slice $\triangle \mathbf{t}$ through iterative projection method. We assume that $\triangle t_k^{n_i}$ is the ith HRIS time slice at n_i iterations, and its projected time slice $\triangle t_i^{\grave{n}_i}$ is represented as:

$$\triangle t_i^{\grave{n}_i} = \triangle t_i^{n_i} \left(1 + \alpha_i \frac{R - R_i^{n_i}}{\sum_{k=1}^{N_T} |R - R_k|}\right), \tag{52}$$

where α_i is the projection factor. The projection time slice $\triangle t_i^{\grave{n}_i}$ is obtained by projecting the achievable rate onto the time slice $\triangle t_i^{n_i}$. When $R_i^{n_i} \geq R$, the projection time slice $\triangle t_i^{\grave{n}_i}$ is less than $\triangle t_i^{n_i}$. However, the total sum of the projected time slices $\triangle t_i^{\grave{n}_i}$ does not equal to the period T, so the next iteration time slice $\triangle t_i^{n_i+1}$ is obtained by normalization:

$$\triangle t_i^{n_i+1} = \frac{\triangle t_i^{\grave{n}_i} T}{\sum_{k=1}^{N_T} \triangle t_k^{\grave{n}_i}}. \tag{53}$$

By continuously iterating, the time slice $\triangle t$ is optimized until it exceeds the allowed number of steps.

C. Pseudocode for Adaptive Block Coordinate Descent Algorithm

Algorithm 1 alternates two blocks to minimize $\mathcal{L}_\beta$ in (34): an Adagrad update of $\boldsymbol{\rho}$ using Proposition 1 with per-element step-sizes $\eta_{k,lu}$ (37) and the thresholded binary rule (38), followed by a projection update of $\boldsymbol{\Delta t}$ via (52) and normalization (53). To reduce per-cycle complexity, we adopt an event-triggered scheme with warm start: initialize with the previous solution $(\boldsymbol{\rho}^{n_i}, \boldsymbol{\Delta t}^n)$ and form an active set:

$$\mathcal{I}_{n_i} = \begin{Bmatrix} R_k < R + \eta_R, & \text{or} \\ \mathcal{P}_k\left(\mathbf{p}|\boldsymbol{\rho}, \triangle \mathbf{t}\right) > \tau_{\text{SPEB}}, & \text{or} \\ \|\hat{\mathbf{p}}_k - \tilde{\mathbf{p}}_k\| > d_{\max}, & \\ k \in \mathcal{N}_\mathcal{T}, & \end{Bmatrix} \tag{54}$$

where $\tilde{\mathbf{p}}_i$ is a one-step constant-velocity Kalman prediction and $\eta_R, \tau_{\text{SPEB}}, d_{\max}$ are thresholds. We then run one ABCD step only on $\{\rho_i, \Delta t_i\}_{i \in \mathcal{I}_{n_i}}$ and freeze the others, preserving responsiveness while limiting control overhead.

Algorithm 1: Adaptive Block Coordinate Descent (ABCD) With Event Triggers.

Input: Observation $\hat{\mathbf{y}}$; thresholds $\eta_R,\ \tau_{\text{SPEB}},\ d_{\max}$.
Output: HRIS reflectivity $\boldsymbol{\rho}$; per-HRIS time slices $\{\Delta t_i\}$, $i \in \mathcal{N}_\mathcal{T}$.
Warm start: $(\boldsymbol{\rho}^0, \boldsymbol{\Delta t}^0) \leftarrow$ previous cycle (else random).
for outer iterations $n_i = 1 : N_i$ **do**
  Active set: build $\mathcal{I}_{n_i}$ (54).
  %%%%% Adagrad update for $\boldsymbol{\rho}$ %%%%%
  for Adagrad inner iterations $n_a = 1 : N_a$ **do**
    for HRIS $i \in \mathcal{I}_{n_i}$, rows $l = 1 : N_{\text{row}}$, columns $u = 1 : N_{\text{col}}$ **do**
      Compute $\nabla_{[\boldsymbol{\rho}_i]_{[l,u]}} \operatorname{tr}\{\mathbf{J}\}$ (39);
      Accumulate $\chi_{i,lu} \leftarrow \chi_{i,lu} + (\nabla_{[\boldsymbol{\rho}_i]_{[l,u]}} \operatorname{tr}\{\mathbf{J}\})^2$ (36);
      Set $\eta_{i,lu} = \eta / \sqrt{\chi_{i,lu} + \epsilon}$ (37);
      Update $[\boldsymbol{\rho}_i]_{[l,u]}$ using the thresholded rule (38);
    end for
  end for
  %%%%% Iterative projection for $\boldsymbol{\Delta t}$ %%%%%
  for projection iterations $n_p = 1 : N_p$
    for HRIS $i \in \mathcal{I}_{n_i}$
      $\grave{\Delta t}_i \leftarrow \Delta t_i (1 + \alpha_k \frac{R - R_i}{\sum_k |R - R_k|})$ (52);
    end for
    Normalize: $\Delta t_i \leftarrow \frac{\grave{\Delta t}_i T}{\sum_k \grave{\Delta t}_k}$ for all i (53);
  end for
end for

D. Complexity Analysis

During the optimization, we iterate ABCD N_i times. In each iteration, the Adagrad gradient descent method iterates N_a times. Therefore, the total complexity of the Adagrad gradient descent method is $\mathcal{O}(N_T N_i N_a)$. Similarly, in each iteration of ABCD, the iterative projection method is iterated N_p times. For the iterative projection method, the complexity is mainly affected by the AR of each HRIS. For the AR operation in (8), we use Simpson integration to split the definite integral into n_s small intervals and calculate the complexity of the AR operation as $\mathcal{O}(N_T n_s)$. Therefore, in ABCD, the total complexity of the iterative projection method is $\mathcal{O}(N_p N_i {N_T}^2 n_s)$. The complexity of ABCD is $\mathcal{O}(N_T N_i N_{row} N_{col} + N_i {N_T}^2 N_p n_s)$. As a comparison, the complexity of greedy algorithm is $\mathcal{O}(N_i 2 N_T N_{row} N_{col} ({N_T}^3 + {N_T}^2 n_s))$, the complexity of GA

$$\left[\nabla_{[\boldsymbol{\rho}_k]_{[l,u]}} \nabla_{\mathbf{p}_i} \hbar_k(t)^{\mathrm{T}} \mathbf{s}\right]_{[x]} = \sum_{w=1}^{N_A} s_w \nabla_{[\mathbf{p}_i]_{[x]}} \bar{h}_{wi}^{[0]}(t) \nabla_{[\boldsymbol{\rho}_k]_{[l,u]}} \bar{h}_{wk}^{[i]}(t) + s_w \bar{h}_{wi}^{[0]}(t) \nabla_{[\boldsymbol{\rho}_k]_{[l,u]}} \nabla_{[\mathbf{p}_i]_{[x]}} \bar{h}_{wk}^{[i]}(t), \tag{45}$$

$$\left[\nabla_{[\boldsymbol{\rho}_i]_{[l,u]}} \nabla_{\mathbf{p}_i} \hbar_i(t)^{\mathrm{T}} \mathbf{s}\right]_{[x]} = \sum_{w=1}^{N_A} \sum_{k \neq i}^{N_T} s_w \bar{h}_{wk}^{[0]}(t) \nabla_{[\boldsymbol{\rho}_i]_{[l,u]}} \nabla_{[\mathbf{p}_i]_{[x]}} \bar{h}_{wi}^{[k]}(t) + s_w \nabla_{[\boldsymbol{\rho}_i]_{[l,u]}} \nabla_{[\mathbf{p}_i]_{[x]}} h_{wi}^{[0]}(t), \tag{48}$$

and PSO algorithm is $\mathcal{O}(N_i N_u({N_T}^3 + {N_T}^2 n_s))$, and the complexity of ARO algorithm is $\mathcal{O}(N_i {N_u}^2({N_T}^3 + {N_T}^2 n_s))$,where N_u is the population size.

E. Convergence and Feasibility

With the unified penalized objective $\mathcal{L}_\beta$, our ABCD alternates between ($\mathbb{P}_3^*$) and ($\mathbb{P}_3^{**}$), each equipped with a monotone acceptance rule. Thus $\{\mathcal{L}_\beta(\rho, \Delta t)\}$ is not increasing. Under the assumptions that $f(\hat{\mathbf{y}} \mid \mathbf{p})$ and R_i satisfy standard smoothness and the associated level sets are bounded, any limit point is a stationary point of the penalized problem.

VI. ATDM Cycle Time Slice Budget and Robust Tightening of Uncertainty

We discuss a time slice budget and update strategy for dual time scale ATDM, and tighten uncertainty with equivalent SINR and opportunity constraints to ensure robust feasibility of reachability and localization.

A. Time Budgeting Per ATDM Cycle

We adopt a two-timescale design: a physical layer time slot of length T_{slot} that comprises slice transmission, channel estimation, and data transmission, and an ATDM cycle of length $T = K_{\text{slot}} T_{\text{slot}}$ during which we update the reflectivity and time slices allocation. With Doppler $f_D = v/\lambda$ and coherence time $T_c \approx 0.423/f_D$, we choose $T_{\text{slot}} \leq 0.5 T_c$. There is a negative correlation between speed v and period T. Each ATDM slice Δt_i comprises:

$$\Delta t_i = \underbrace{\tau_{\text{ce},i}}_{\text{channel estimation}} + \underbrace{\tau_{\text{loc},i}}_{\text{localization}} + \underbrace{\tau_{\text{ctrl}}}_{\text{control}} + \underbrace{\tau_{\text{data},i}}_{\text{data}}, \tag{55}$$

where $\sum_k \Delta t_i = T$. For least squares type channel estimation with target mean square error (NMSE) ε_{ce}, a slice length $\tau_p \geq \sigma^2/(P_{\text{tx}} \varepsilon_{\text{ce}})$ is sufficient, where P_{tx} is the power of data transmission. If N_A anchors transmit slices and the active HRIS uses K training reflection patterns, then $\tau_{\text{ce},k} \approx (N_A + K)\, \tau_p$. Localization slice $\tau_{\text{loc},i}$ uses a fixed fraction $s_{\text{loc}} \in [0.1, 0.25]$ of Δt_i. Control slice $\tau_{\text{ctrl}} \approx H/R_{\text{ctrl}}$ is typically $\ll 0.1$ ms and amortized across slices, where H bits for reflectivity map updates. When achievable rate is measured on the data sub-interval, and the constraint $R_i \geq R$ implies a minimum data achievable rate:

$$\tau_{\text{data},i} \geq \Delta t_i \, \frac{R}{\log_2(1 + \text{SINR}_i)}. \tag{56}$$

Hence each slice must satisfy the feasibility lower bound:

$$\Delta t_i \geq \frac{\tau_{\text{ce},i} + \tau_{\text{loc},i} + \tau_{\text{ctrl}}}{1 - R/\log_2(1 + \text{SINR}_i)}, \tag{57}$$

and our iterative projection step enforces the intersection of $\sum_i \Delta t_i = T$ with these slice lower bounds. Finally, the reflectivity update frequency follows $f_{\text{upd}} \in [1/(T_c),\, 1/(0.2T_c)]$ for mmWave.

TABLE II
Key System Parameters

Symbol	Value
Region $\mathcal{A}$	$100 \times 100 \times 5$ m^3
Carrier frequency f_c	24 GHz
Transmission period T	1 s
Number of base stations N_{BS}	4
BS coordinates $\mathbf{b}_i$	$(0,0,5)$,$(100,0,5)$,$(0,100,5)$,$(100,100,5)$
Receiver SNR	20 dB
HRIS unit spacing	11.5 mm
HRIS unit area	11.5×11.5 mm^2
BS / HRIS gains G_a, G_g	1
Channel model	LOS free-space
Noise model	AWGN consistent with target SNR
HRIS size	$N_{\text{row}} \times N_{\text{col}}$

B. Uncertainty Models and Tightening

Let the data SINR be uncertain due to CE error and fast fading: $\text{SINR}_i = \bar{\gamma}_i + \delta\gamma_i$ with $\mathbb{E}[\delta\gamma_i] = 0$, $\text{Var}[\delta\gamma_i] = \sigma^2_{\gamma,i}$. Using an error-as-noise bound, the effective SINR satisfies

$$\gamma_i^{\text{eff}} \;\geq\; \frac{\bar{\gamma}_i}{1 + \varepsilon_{\text{ce}}\, \bar{\gamma}_i}, \tag{58}$$

where ε_{ce} is the CE normalized NMSE. We impose a chance constrained AR requirement, which is enforced by the deterministic tightening:

$$\frac{\tau_{\text{data},i}}{\Delta t_i} \log_2\!\big(1 + \gamma_i^{\text{eff}}\big) \;\geq\; R + \zeta_\epsilon\, \sigma_{R,i}, \tag{59}$$

where $\sigma_{R,i}$ is the standard deviation of the rate and ζ_ϵ is the normal quantile (e.g., 1.64 for 95%). Equivalently, the slice lower bound becomes tighter by replacing SINR_i with γ_i^{eff} and adding the margin $\zeta_\epsilon \sigma_{R,i}$.

VII. Simulations

Simulations evaluate the key factors of the HRIS-V2X system: the number of HRISs, the number of HRIS reflective units, the number of bits per reflective unit, and the AR achievement rate of the HRIS-V2X system. We compare our proposed ABCD with GA [47], greedy algorithm (GDY) [48], PSO [49] and ARO [50]. In addition, we analyze the impact of HRIS phase modulation on the HRIS-V2X system. All simulation results are obtained by averaging over 500 random HRIS placements. The simulation parameters are listed in Table II. Unless specified, these parameters remain unchanged.

A. HRIS Number Evaluation

Fig. 4 jointly plots the average localization error (left axis, SPEB in m^2) and the proportion of HRIS whose AR satisfies the constraint (right axis, %) versus the number of HRIS. The AR constraint is set to $R = 0.18$ (bits/s/Hz/bandwidth). Across the whole range, the ABCD algorithm consistently yields the lowest SPEB and the highest AR-constraint satisfaction rate among GA, GDY, PSO, and ARO, where we attribute to the ABCD algorithm's lower complexity, allowing more reflective-unit parameters to be optimized under the same compute budget. As the number of HRIS increases, the communication time

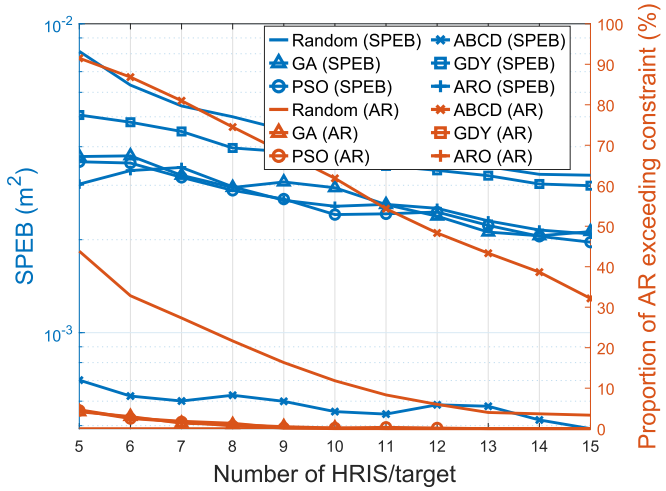

Fig. 4. AR-constraint exceeding rate and squared position error bound (SPEB) versus the number of HRIS. Left y-axis: SPEB, m^2. Right y-axis: AR-constraint exceeding rate.

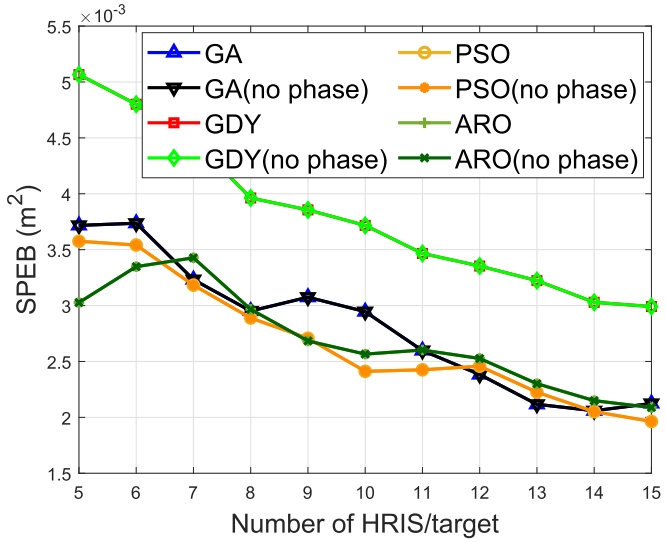

Fig. 5. Effect of HRIS phase modulation on localization accuracy: SPEB (m^2) versus the number of HRIS. For each algorithm (GA, GDY, PSO, ARO), the 'NO PHASE' curves closely overlap their phase-modulated counterparts, showing that phase modulation has little impact on SPEB in the considered HRIS-V2X setup.

allocated to each HRIS within a cycle shrinks, reducing its AR. Meanwhile, for each target, localization is completed in a short period of time, manifested as more targets assisting each other in localization, resulting in a gradual decrease in SPEB, thereby improving localization accuracy with the increased number of HRIS.

B. Phase Modulation Evaluation

Fig. 5 highlights the effect of HRIS phase modulation by contrasting localization accuracy SPEB with and without phase modulation for each algorithm (GA, GDY, PSO, and ARO). The metric is the average SPEB (m^2) plotted against the number of HRIS. Across all HRIS counts, the paired curves nearly overlap, indicating that enabling phase modulation yields negligible improvement in localization accuracy under our HRIS-V2X system.

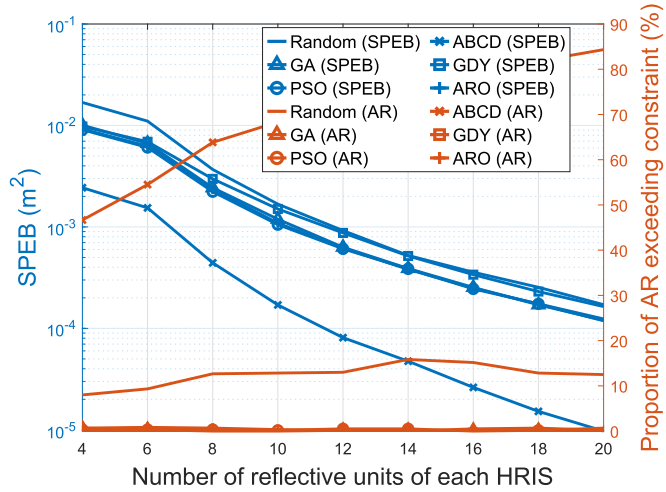

Fig. 6. AR-constraint exceeding rate and squared position error bound (SPEB) versus the number of reflective units of each HRIS. Left y-axis: SPEB, m^2. Right y-axis: AR-constraint exceeding rate.

C. Reflective Units Number Evaluation

Fig. 6 jointly plots localization accuracy and AR-constraint satisfaction versus the number of reflective units per HRIS: the left y-axis shows the SPEB (m^2), and the right y-axis shows the proportion of HRIS whose AR is at least R (the AR constraint). With a fixed compute budget, ABCD achieves markedly lower SPEB than GA, GDY, PSO, and ARO because its lower complexity allows more parameters of the reflective units to be optimized; in particular, compared with GDY, ABCD reduces the average SPEB by 91.79%. As the number of reflective units increases, each HRIS can reflect and receive more signals within one cycle, and extract richer localization information, while the decrease in SPEB indicates an improvement in localization accuracy. Further, as the number of HRIS reflective units increases, each HRIS can receive more communication signals in one cycle, improving communication efficiency and enhancing AR constraint satisfaction rate.

D. Runtime and Accuracy Distribution

Fig. 7 reports the averaged simulation time for each optimization, which varies with the number of HRIS. As illustrated, ABCD is consistently the fastest, followed by ARO/PSO and then GA, while GDY incurs the highest cost. The runtime increases monotonically with the HRIS units, reflecting the growth in optimized variables. All timings are measured in MATLAB R2023b on a PC equipped with an Intel Core i9-13900 K CPU.

Fig. 8 indicates the CDF of localization error measured by SPEB (m^2) over 500 random HRIS placements. Curves that lie further to the left correspond to lower errors. ABCD achieves the most favorable distribution (leftmost curve), GA/PSO/ARO

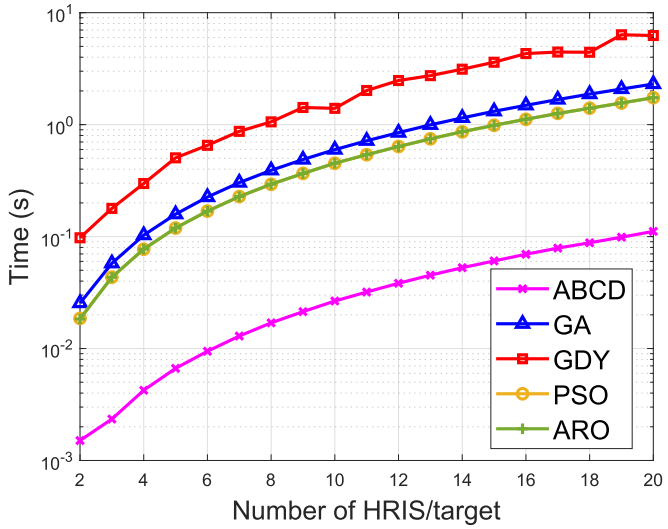

Fig. 7. Runtime scaling with the number of HRIS (MATLAB R2023b, Intel Core i9-13900 K). ABCD is consistently the fastest, followed by ARO/PSO and GA, while GDY incurs the highest cost.

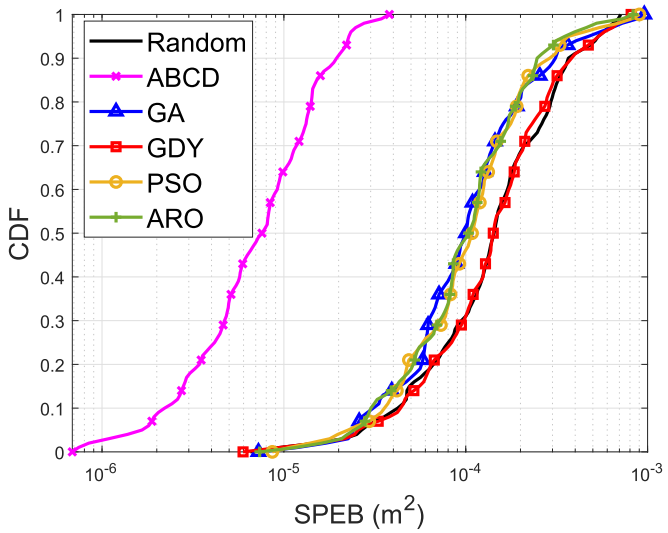

Fig. 8. CDF of SPEB (m^2) over 300 random HRIS placements. Curves farther to the left indicate lower localization error; ABCD shows the most favorable distribution.

form a close middle group, GDY is noticeably worse, and the random baseline is far to the right. In summary, these results indicate that ABCD offers a superior speed-accuracy performance with the same settings.

VIII. Conclusion

In V2X systems, the use of HRIS for high-precision localization is very promising, but the control and communication constraints of HRIS are quite complex. In this paper, we propose the 6G V2X system with HRIS in cooperative localization. In the HRIS-V2X system, base stations and mobile HRIS form a communication and localization network to provide services for vehicles. We design the localization and communication protocol for the 6G V2X system, which integrates localization, communication, channel estimation, and parameter modification into each cycle. However, optimizing the localization accuracy in the HRIS-V2X system is a non convex NP problem. We propose ABCD, which can simultaneously optimize the reflectivity modulation and time-division multiplexing protocol of HRIS to improve localization accuracy. The simulation results of the HRIS-V2X system demonstrate that the optimization impact of the ABCD algorithm is affected by the number of HRIS and the number of reflection units. In addition, ABCD achieves a 94.1% reduction in SPEB optimization compared to greedy algorithm, a 91.9% reduction compare to GA, a 91.8% reduction compare to ARO, and a 92.1% reduction compare to PSO.

References

[1] M. Noor-A-Rahim et al., "6G for Vehicle-to-Everything (V2X) communications: Enabling technologies, challenges, and opportunities," *Proc. IEEE*, vol. 110, no. 6, pp. 712–734, Jun. 2022.

[2] H. Kim, S. H. Lee, and S. Kim, "Cooperative localization with constraint satisfaction problem in 5G vehicular networks," *IEEE Trans. Intell. Transp. Syst.*, vol. 23, no. 4, pp. 3180–3189, Apr. 2022.

[3] K. Viana, A. Zubizarreta, and M. Dıéz, "Robust localization for autonomous vehicles in dense urban areas," in *Proc. 25th Int. Conf. Syst. Theory, Control Comput.*, 2021, pp. 107–112.

[4] P. Schorner, M. Conzelmann, T. Fleck, M. Zofka, and J. M. Zollner, "Park my car! automated valet parking with different vehicle automation levels by V2X connected smart infrastructure," in *Proc. IEEE Int. Intell. Transp. Syst. Conf.*, 2021, pp. 836–843.

[5] L. Gao et al., "Cooperative localization in transportation 5.0," *IEEE Trans. Intell. Veh.*, vol. 9, no. 3, pp. 4259–4264, Mar. 2024.

[6] R. Yang, C.-X. Wang, J. Huang, E.-H. M. Aggoune, and Y. Hao, "A novel 6G ISAC channel model combining forward and backward scattering," *IEEE Trans. Wireless Commun.*, vol. 22, no. 11, pp. 8050–8065, Nov. 2023.

[7] A. Ihsan, W. Chen, S. Zhang, and S. Xu, "Energy-efficient NOMA multicasting system for beyond 5G cellular V2X communications with imperfect CSI," *IEEE Trans. Intell. Transp. Syst.*, vol. 23, no. 8, pp. 10721–10735, Aug. 2022.

[8] E. Leoni et al., "Validating vehicular localization indoor using UWB: Challenges and solutions," in *Proc. 9th Int. Workshop Adv. Sensors Interfaces*, 2023, pp. 27–32.

[9] J. Choi and J. H. Cho, "A joint optimization of pilot and phase shifts in uplink channel estimation for hybrid RIS-aided multi-user communication systems," *IEEE Trans. Veh. Technol.*, vol. 73, no. 4, pp. 5197–5212, Apr. 2024.

[10] M. Li, S. Zhang, Y. Ge, F. Gao, and P. Fan, "Joint channel estimation and data detection for hybrid RIS aided millimeter wave OTFS systems," *IEEE Trans. Commun.*, vol. 70, no. 10, pp. 6832–6848, Oct. 2022.

[11] K. Zhang, N. Ma, X. Yang, K. Peng, Y. Chen, and S. Liu, "A novel wideband geometry-based channel model for HRIS-assisted THz inter-room communications," in *Proc. IEEE/CIC Int. Conf. Commun. China*, 2024, pp. 1187–1192.

[12] W. He, C. Hu, Y. Xu, and Y. Li, "Joint DFBS beamforming and HRIS beamforming for HRIS-aided ISAC systems," in *Proc. IEEE/CIC Int. Conf. Commun. China*, 2024, pp. 1443–1448.

[13] S. Gyawali, S. Xu, Y. Qian, and R. Q. Hu, "Challenges and solutions for cellular based V2X communications," *IEEE Commun. Surv. Tut.*, vol. 23, no. 1, pp. 222–255, Firstquarter 2021.

[14] M. Z. Win, R. M. Buehrer, G. Chrisikos, A. Conti, and H. V. Poor, "Foundations and trends in localization technologies — Part I," *Proc. IEEE*, vol. 106, no. 6, pp. 1019–1021, Jun. 2018.

[15] M. Z. Win, Y. Shen, and W. Dai, "A theoretical foundation of network localization and navigation," *Proc. IEEE*, vol. 106, no. 7, pp. 1136–1165, Jul. 2018.

[16] J. Chen, W. Dai, Y. Shen, V. K. N. Lau, and M. Z. Win, "Resource management games for distributed network localization," *IEEE J. Sel. Areas Commun.*, vol. 35, no. 2, pp. 317–329, Feb. 2017.

[17] T. Wang, A. Conti, and M. Z. Win, "Network navigation with scheduling: Distributed algorithms," *IEEE/ACM Trans. Netw.*, vol. 27, no. 4, pp. 1319–1329, Aug. 2019.

[18] B. Peng, G. Seco-Granados, E. Steinmetz, M. Fröhle, and H. Wymeersch, "Decentralized scheduling for cooperative localization with deep reinforcement learning," *IEEE Trans. Veh. Technol.*, vol. 68, no. 5, pp. 4295–4305, May 2019.
[19] T. Zhang, A. F. Molisch, Y. Shen, Q. Zhang, H. Feng, and M. Z. Win, "Joint power and bandwidth allocation in wireless cooperative localization networks," *IEEE Trans. Wireless Commun.*, vol. 15, no. 10, pp. 6527–6540, Oct. 2016.
[20] L. Yin, Q. Ni, and Z. Deng, "Intelligent multisensor cooperative localization under cooperative redundancy validation," *IEEE Trans. Cybern.*, vol. 51, no. 4, pp. 2188–2200, Apr. 2021.
[21] C. Fan, L. Li, M.-M. Zhao, A. Liu, and M.-J. Zhao, "Communication and energy-constrained neighbor selection for distributed cooperative localization," *IEEE Trans. Wireless Commun.*, vol. 22, no. 6, pp. 4158–4172, Jun. 2023.
[22] C. Gaudreauand and A. Chaaban, "Localization by modulated reconfigurable intelligent surfaces," *IEEE Commun. Lett.*, vol. 26, no. 12, pp. 2904–2908, Dec. 2022.
[23] M. Luan, B. Wang, Z. Chang, T. Hämäläinen, Z. Ling, and F. Hu, "Joint subcarrier and phase shifts optimization for RIS-aided localization-communication system," in *Proc. IEEE 95th Veh. Technol. Conf.*, 2022, pp. 1–5.
[24] M. Mizmizi, R. A. Ayoubi, D. Tagliaferri, K. Dong, G. G. Gentili, and U. Spagnolini, "Conformal metasurfaces: A novel solution for vehicular communications," *IEEE Trans. Wireless Commun.*, vol. 22, no. 4, pp. 2804–2817, Apr. 2023.
[25] Y. He et al., "Air-to-ground integrated internet of vehicles enhanced by lapss and RISs: Location, power, and phase shift optimization," *IEEE Internet Things J.*, vol. 11, no. 10, pp. 18020–18034, May 2024.
[26] Y. U. Ozcan, O. Ozdemir, and G. K. Kurt, "Reconfigurable intelligent surfaces for the connectivity of autonomous vehicles," *IEEE Trans. Veh. Technol.*, vol. 70, no. 3, pp. 2508–2513, Mar. 2021.
[27] Y. Mao et al., "A high-capacity MAC protocol for UAV-enhanced RIS-assisted V2X architecture in 3-D IoT traffic," *IEEE Internet Things J.*, vol. 11, no. 13, pp. 23711–23726, Jul. 2024.
[28] X. Gu, W. Duan, G. Zhang, Y. Ji, M. Wen, and P.-H. Ho, "Socially aware V2X networks with RIS: Joint resource optimization," *IEEE Trans. Veh. Technol.*, vol. 71, no. 6, pp. 6732–6737, Jun. 2022.
[29] G. Singh, A. Srivastava, and V. A. Bohara, "Visible light and reconfigurable intelligent surfaces for beyond 5G V2X communication networks at road intersections," *IEEE Trans. Veh. Technol.*, vol. 71, no. 8, pp. 8137–8151, Aug. 2022.
[30] B. Ji et al., "Cooperative transmission algorithm of RIS-assisted intelligent transportation system under aggregated interference," *IEEE Trans. Intell. Transp. Syst.*, vol. 26, no. 10, pp. 17280–17291, Oct. 2025.
[31] M. Mizmizi, D. Tagliaferri, D. Badini, and U. Spagnolini, "Target-to-user association in ISAC systems with vehicle-lodged RIS," *IEEE Wireless Commun. Lett.*, vol. 12, no. 9, pp. 1558–1562, Sep. 2023.
[32] X. Long, Y. Zhao, H. Wu, and C.-Z. Xu, "Deep reinforcement learning for integrated sensing and communication in RIS-assisted 6G V2X system," *IEEE Internet Things J.*, vol. 11, no. 24, pp. 39834–39849, Dec. 2024.
[33] R. Ghazalian, H. Chen, G. C. Alexandropoulos, G. Seco-Granados, H. Wymeersch, and R. Jäntti, "Joint user localization and location calibration of a hybrid reconfigurable intelligent surface," *IEEE Trans. Veh. Technol.*, vol. 73, no. 1, pp. 1435–1440, Jan. 2024.
[34] R. Ghazalian, G. C. Alexandropoulos, G. Seco-Granados, H. Wymeersch, and R. Jantti, "Joint 3D user and 6D hybrid reconfigurable intelligent surface localization," *IEEE Trans. Veh. Technol.*, vol. 73, no. 10, pp. 15302–15317, Oct. 2024.
[35] X. Zhang and H. Zhang, "Hybrid reconfigurable intelligent surfaces-assisted near-field localization," *IEEE Commun. Lett.*, vol. 27, no. 1, pp. 135–139,Jan. 2023.
[36] M. Li, S. Zhang, Y. Ge, Z. Li, F. Gao, and P. Fan, "Star-RIS aided integrated sensing and communication over high mobility scenario," *IEEE Trans. Commun.*, vol. 72, no. 8, pp. 4788–4802, Aug. 2024.
[37] D. K. Pin Tan et al., "Integrated sensing and communication in 6G: Motivations, use cases, requirements, challenges and future directions," in *Proc. 1st IEEE Int. Online Symp. Joint Commun. Sens.*, 2021, pp. 1–6.
[38] X. Hu, R. Zhang, and C. Zhong, "Semi-passive elements assisted channel estimation for intelligent reflecting surface-aided communications," *IEEE Trans. Wireless Commun.*, vol. 21, no. 2, pp. 1132–1142, Feb. 2022.
[39] S. Zhang, S. Zhang, F. Gao, J. Ma, and O. A. Dobre, "Deep learning optimized sparse antenna activation for reconfigurable intelligent surface assisted communication," *IEEE Trans. Commun.*, vol. 69, no. 10, pp. 6691–6705, Oct. 2021.
[40] K. Zhi, C. Pan, H. Ren, K. K. Chai, and M. Elkashlan, "Active RIS versus passive RIS: Which is superior with the same power budget?," *IEEE Commun. Lett.*, vol. 26, no. 5, pp. 1150–1154,May 2022.
[41] C. Zhang, W. Chen, C. He, and X. Li, "Throughput maximization for intelligent reflecting surface-aided device-to-device communications system," *J. Commun. Inf. Netw.*, vol. 5, no. 4, pp. 403–410, 2020.
[42] X. Qian, X. Hu, C. Liu, M. Peng, and C. Zhong, "Sensing-based beamforming design for joint performance enhancement of RIS-aided ISAC systems," *IEEE Trans. Commun.*, vol. 71, no. 11, pp. 6529–6545, Nov. 2023.
[43] Z. Xing, R. Wang, and X. Yuan, "Joint active and passive beamforming design for reconfigurable intelligent surface enabled integrated sensing and communication," *IEEE Trans. Commun.*, vol. 71, no. 4, pp. 2457–2474, Apr. 2023.
[44] F. Nassar, K. Singh, S. Prakriya, B. Hazarika, C.-P. Li, and Z. Ding, "Dynamic user clustering and backscatter-enabled RIS-assisted NOMA ISAC," *IEEE Trans. Wireless Commun.*, vol. 23, no. 8, pp. 9173–9189, Aug. 2024.
[45] C. Liao, F. Wang, G. Han, Y. Huang, and V. K. N. Lau, "Beamforming design for hybrid active-passive RIS assisted integrated sensing and communications," *IEEE Commun. Lett.*, vol. 27, no. 11, pp. 2938–2942, Nov. 2023.
[46] W. Hao, Y. Qu, S. Zhou, F. Wang, Z. Lu, and S. Yang, "Joint beamforming design for hybrid RIS-assisted mmWave ISAC system relying on hybrid precoding structure," *IEEE Internet Things J.*, vol. 11, no. 18, pp. 29455–29469, Sep. 2024.
[47] K. Zhang, C. Liu, H. Wang, and Y. Song, "An IRS-aided mmWave massive MIMO systems based on genetic algorithm," in *Proc. IEEE 20th Int. Conf. Commun. Technol.*, 2020, pp. 288–293.
[48] H. Zhang et al., "RSS fingerprinting based multi-user outdoor localization using reconfigurable intelligent surfaces," in *Proc. 15th Int. Symp. Med. Inf. Commun. Technol.*, 2021, pp. 167–172.
[49] J. Kennedy and R. Eberhart, "Particle swarm optimization," in *Proc. Int. Conf. Neural Netw.*, 1995, pp. 1942–1948.
[50] Q. Pu, X. Lan, M. Zhou, F. Jiang, R. Cai, and L. Guo, "RIS-aided indoor positioning system based on passive reflective elements optimization," *IEEE Trans. Veh. Technol.*, vol. 73, no. 11, pp. 17095–17105, Nov. 2024.

Ziyang Lu received the BS degree from Jilin University, in 2020, and the PhD degree from Sun Yat-Sen University, in 2025. He is currently a postdoctoral researcher with the School of Electronic and Information Engineering, South China University of Technology, Guangzhou, China. His research interests include reconfigurable intelligent surface and its applications.

Yubin Zhao (Senior Member, IEEE) received the BS and MS degrees from the Beijing University of Posts and Telecommunications, Beijing, China, in 2007 and 2010, respectively, and the PhD degree in computer science from Freie Universität Berlin , Berlin, Germany, in 2014. He was with Center for Cloud Computing as an associate professor, Shenzhen Institutes of Advanced Technology, Chinese Academy of Sciences, Shenzhen, China, in 2014. He is currently an associate professor with the School of Microelectronics Science and Technology, Sun Yat-Sen University, Zhuhai, China. His research interest include wireless power transfer, indoor localization, and target tracking. He is the guest editor and reviewer for several journals. He was the recipient of IEEE distinguished service award in IEEE SmartData 2023 and Excellent Teacher Award of College Computing Science in China, 2023. He is the vice technical chair of IEEE SmartData 2023, IEEE ScalCom 2022, publicity chair of IEEE NFV-SDN 2019 and tutorial chair of IEEE NFV-SDN 2020.

Xiaofan Li (Senior Member, IEEE) received the BS and PhD degrees from the Beijing University of Posts and Telecommunication in 2007 and 2012, respectively. From 2010 to 2011, she studied in University of Washington as an exchanged Ph.D student. She joined the State Radio Monitoring Center and Testing Center (SRTC), from 2012, and was transferred to SRTC Shenzhen Lab, from 2013. She is currently an associate professor with the School of Intelligent Systems Science and Engineering, Jinan University, Zhuhai, China. Her research interests include interference analysis among different radio systems, testing and evaluation methods for innovative radio technologies, cooperative communication, cognitive radio, Internet of Things, and radio management strategy.

Huaming Wu (Senior Member, IEEE) received the BE and MS degrees in electrical engineering from the Harbin Institute of Technology, China, in 2009 and 2011, respectively, and the PhD degree with the highest honor in computer science, Freie Universität Berlin, Germany, in 2015. He is currently an associate professor with the Center for Applied Mathematics, Tianjin University, China. His research interests include model-based evaluation, wireless and mobile network systems, mobile cloud computing, and deep learning.

Cheng-Zhong Xu (Fellow, IEEE) received the PhD degree from the University of Hong Kong in 1993. He was in the faculty of Wayne State University and Shenzhen Institutes of Advanced Technology of CAS. He is currently a chair professor of computer science with the University of Macau, China. He has authored or coauthored two research monographs and more than 400 journal and conference papers and received more than 13000 citations. His research interests include cloud and distributed computing, systems support for AI, smart city, and autonomous driving. He was a Best Paper Awardee or Nominee of conferences, including HPCA'2013, HPDC'2013, Cluster'2015, ICPP'2015, GPC'2018, UIC'2018, and HPBD&IS'2019. He was also a co-inventor of more than 120 patents and a co-founder of Shenzhen Institute of Baidou Applied Technology. He serves or served on a number of journal editorial boards, including IEEE *Transactions on Computers*, IEEE *Transactions on Cloud Computing*, IEEE *Transactions on Parallel and Distributed Systems*, *JPDC*, *Science China*, and *ZTE Communication*. Prof. Xu was the chair of IEEE Technical Committee on Distributed Processing, from 2015 to 2020. He was the recipient of the Faculty Research Award, Career Development Chair Award, and the President's Award for Excellence in Teaching of WSU. He was also the recipient of "Outstanding Oversea Scholar" award of NSFC.

Quan Xue (Fellow, IEEE) received the BS, MS, and PhD degrees in electronic engineering from the University of Electronic Science and Technology of China (UESTC), Chengdu, China, in 1988, 1990, and 1993, respectively. In 1993, he was with UESTC, as a lecturer, where he became professor, in 1997. From 1997 to 1998, he was a research associate and then research fellow with The Chinese University of Hong Kong, Hong Kong. In 1999, he was with the City University of Hong Kong (CityU), Hong Kong, where he was the chair professor of microwave engineering, from 2013 to 2017. He was an associate vice president of CityU, Innovation Advancement and China Office, from 2011 to 2015, director of the Information and Communication Technology Center, Hong Kong, and deputy director of State Key Laboratory of Millimeter Waves, Hong Kong. He is currently the dean of the School of Electronic and Information Engineering, South China University of Technology, Guangzhou, China. He has authored or coauthored more than 350 internationally refereed journal articles and more than 170 international conference papers. He is a co-inventor of five granted Chinese patents and 27 granted U.S. patents (five of them have been licensed), in addition to 29 filed patents. His research interests include microwave/millimeter wave/terahertz passive components, active components, antenna, microwave monolithic integrated circuits, and radio frequency integrated circuits. Dr. Xue was an administrative committee member for IEEE Microwave Theory and Techniques Society, from 2011 to 2013. He was the recipient of the 2017 H. A. Wheeler Paper Award of IEEE Antenna and Propagation Society. He was an associate editor of IEEE *Transactions on Microwave Theory and Techniques,* from 2010 to 2013, IEEE *Transactions on Industrial Electronics*, from 2010 to 2015, and IEEE *Transactions on Antennas and Propagation*, from 2016 to 2017. He was an editor of International Journal of Antennas and Propagation, from 2010 to 2013.